Faculty of Physics and Astronomy

University of Heidelberg

Diploma thesis

in Physics

submitted by

Raoul Heyne

born in Wolfenbüttel

October 2008

Creation, diagnostics and manipulation of a non-neutral one-component plasma

This diploma thesis was carried out by Raoul Heyne at the

Max Planck Institute for Nuclear Physics

under the supervision of

Dr. Alban Kellerbauer

Erzeugung, Diagnostik und Manipulation eines nichtneutralen Einkomponentenplasmas:

Das sympathetische Kühlen von Ionen mit Elektronen ist eine etablierte Technik, die routinemäßig bei negativen Teilchen von Antiprotonen bis zu Molekühlen angewendet wird. Ein Elektronenstrahl kann in einer Penningfalle gefangen und als ein nichtneutrales Einkomponentenplasma gespeichert werden. Auf Grund der hohen Zyklotronfrequenz der Elektronen kühlen diese schnell auf die sie umgebene kryogenische Umgebung ab und können somit benutzt werden, um andere Teilchen zu kühlen. Im Rahmen dieser Diplomarbeit wurde eine Elektronenkanone auf der Grundlage einer handelsüblichen Elektronenquelle entworfen, gebaut und in Betrieb genommen. Der daraus entstehende Elektronenstrahl wurde in einer zylindrischen Penningfalle gefangen und für längere Zeit gespeichert. Ein Plasmadiagnosesystem wurde installiert und dazu verwendet, Informationen über alle relevanten Plasmaeigenschaften wie geometrische Ausmaße, Dichte und Teilchenanzahl zu erhalten. Zwei verschiedene Techniken der Plasmaanregung durch sich zeitlich verändernde elektrische Felder wurden verwendet, um das Plasmadiagnosesystem zu testen, die Synchrotronkühlungsrate zu messen und die Plasmaeigenschaften zu verändern. Dadurch wurde eine wesentlich längere Speicherung des Plasmas in der Penningfalle erreicht.

Creation, diagnostics and manipulation of a non-neutral one-component plasma:

The sympathetic cooling of ions with electrons is a well-established technique that is routinely used on negative particles ranging from antiprotons to molecules. An electron beam can be captured and confined in a Penning trap, forming a non-neutral one-component plasma. Due to the high frequency of their cyclotron motion, the electrons then quickly cool to the temperature of the cryogenic environment and can be used as a cooling agent for other particles. In the course of this thesis, an electron gun based on a commercial electron source was designed, built and put into operation. The resulting electron beam was captured in a cylindrical Penning trap and stored for extended periods. A plasma modes diagnostics system was installed and used to obtain information on all relevant plasma properties, such as geometric extent, density and particle number. Two different techniques, both making use of plasma excitation by time-varying electric fields, were used to test the diagnostics system, measure the synchrotron cooling rate, and modify the plasma properties. In this way, a significant increase in the plasma storage time was achieved.

CONTENTS

1. INTRODUCTION AND MOTIVATION

One of the most fundamental problems in physics concerns the relation of matter and antimatter. Two basic theorems relate their properties: The CPT theorem and the weak equivalence principle. The CPT theorem, postulated by Wolfgang Pauli in 1955, states that all laws of physics remain unchanged when the combined operations C (charge conjugation), P (parity – inversion of the spatial coordinates) and T (time reversal) are applied to a system [1]. When the CPT operator is applied to a particle's wavefunction, the antiparticle results. It is also a consequence of this postulate that a particle and its antiparticle have identical fundamental properties, with the sole exception of some quantities, such as the electric charge, having the opposite sign.

CPT invariance has been tested by comparing properties of particles and their antiparticles to high precision [2, 3, 4, 5]. Until today, no deviation from perfect CPT symmetry has been found. Currently several groups are attempting to further test CPT invariance by studying the antihydrogen atom at the antiproton decelerator (AD) at CERN, Geneva [6, 7]. Once sufficient quantities of antiatoms can be captured in neutral-atom traps, it is planned to investigate the atomic 1S–2S transition by Doppler-free laser spectroscopy and to compare the result to the corresponding frequency in ordinary hydrogen, one of the most precise determinations of any fundamental property [8]. Since 2002, experiments at the AD have succeeded in producing millions of antihydrogen atoms [9, 10], but their capture and storage has not yet been achieved.

The weak equivalence principle (WEP) harks back to Galileo Galilei. In 1638, while being persecuted by the Inquisition, he published his law of falling bodies, according to which the inertial and the gravitational mass of a body are equivalent [11]. The theory of general relativity builds on this principle, but with the mass replaced by the stress–energy tensor. General relativity describes gravity as a geometric phenomenon, with four-dimensional spacetime being curved by the masses it contains. However, efforts are being made to formulate gravity as a quantum field theory, in which the force is mediated by an exchange particle, the graviton. The graviton that corresponds to Newtonian gravity is expected to be a spin-2 (tensor) boson. In addition, spin-1 (vector) and/or spin-0 (scalar) bosons could exist, whose effects might cancel out in ordinary matter. The consequences of such additional aspects of the gravitational force would however be dramatic when studying the interaction between matter and antimatter particles. The WEP has been tested to high precision with ordinary matter [12], but not yet at all with antimatter. This is due to the

fact that until recently only charged antimatter particles were available, which are very sensitive to stray electric and magnetic fields.

The goal of an antimatter gravity experiment with neutral antihydrogen, which would circumvent this problem, is currently being pursued by the AEGIS project (Antimatter Experiment: Gravity, Interferometry, Spectroscopy) at CERN/AD which has recently been proposed [13]. Any deviations from the WEP for antimatter would have far-reaching consequences for cosmology and would invalidate the current theory of general relativity, requiring either extensions to the theory or a complete reformulation in terms of a quantum field theory. The proposed AEGIS project is based on the production of antihydrogen by resonant charge exchange of positronium with cold antiprotons. Positrons from a Surko-type source [14] impinge on a nanoporous insulator material, creating thermal positronium [15]. Antihydrogen is then created by resonant charge exchange of the positronium with cold antiprotons [16] and formed into a beam by Stark acceleration with inhomogeneous electric fields [17]. Finally, the acceleration of the antihydrogen atoms in the earth's gravitational field will be measured with a Moiré deflectometer [18] consisting of two material gratings and a position-sensitive detector.

For any precision experiment with antimatter, the availability of samples at the lowest possible temperature is of the utmost importance. One of the most promising routes to cold antihydrogen is the pre-cooling of antiprotons prior to recombination. Since the antiproton mass is roughly 2000 times greater than the electron mass, antihydrogen will then be created close to the temperature of the pre-cooled antiprotons. Antiprotons can easily be cooled to the temperature of a cryogenic environment by electron cooling. Recently, a technique has been proposed that would allow the cooling of antiprotons to much lower temperatures by sympathetic cooling with a negative atomic ion that is laser-cooled [19]. The aim of the UNIC project (Ultracold Negatice Ions by indirect laser Cooling) at the Max Planck Institute for Nuclear Physics is to achieve the first-ever laser cooling of negative ions and to validate this novel technique.

Currently the only known atomic anion amenable to laser cooling is the negative osmium ion, which has a bound excited state with opposite parity from the ground state [20]. Since the excited state is very weakly bound with a binding energy of only 11 meV, the excess electron can become detached in collisions with other ions at temperatures above about 80 K. Hence, the Os^- ions have to be cooled to that temperature before laser cooling can be applied. This can be achieved by sympathetic cooling with electrons in a cryogenic environment, which quickly cool to the temperature of the surrounding Penning trap by synchrotron radiation. The creation of an electron plasma, its capture in a Penning trap, as well as its diagnostics and manipulation are the subject of this diploma thesis.

In particular, the following detailed tasks were to be carried out:

1. To design and build an electron source based on a commercial barium oxide cathode;

2. To capture and confine an electron plasma in the UNIC Penning trap;

3. To set up and test a plasma diagnostics system based on a prototype used at the ATHENA experiment;

4. To test the performance of the diagnostics system by modifying the plasma parameters with radiofrequency and rotating-wall electric fields.

The design, construction and testing of the electron source are detailed in Chapter 3. In Chapter 4, the plasma confinement, and in Chapter 5, the plasma diagnostics and manipulation are described.

2. THEORETICAL BACKGROUND

2.1 Penning traps

A Penning trap is an electromagnetic trap in which charged particles are confined in radial direction by a magnetic field and in axial direction by a three-dimensional electric quadrupole field. Two different types of Penning traps are distinguished: Hyperbolic and cylindrical Penning traps.

The hyperbolic Penning trap contains hyperbolical ring and end cap electrodes as shown in Figure 2.1.

Thereby a three-dimensional electric potential is generated. To get particles into the trap the end caps have to be provided with holes so the particles can be shot into the trap. The end caps are used also to slow down the particles by applying high voltages to them.

For a harmonic potential in the center of the Penning trap, the following potential is needed [21]:

$$\Phi(z) = K\, z^2. \tag{2.1}$$

Using the Poisson equation we get:

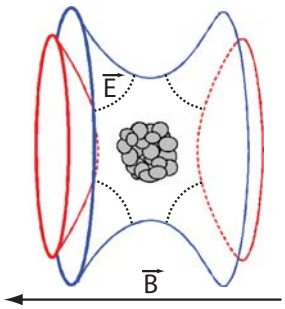

Fig. 2.1: Principle sketch of a hyberbolical Penning trap.

Fig. 2.2: Photograph of a hyperbolical Penning trap.

$$\frac{\partial^2\Phi}{\partial y^2} + \frac{\partial^2\Phi}{\partial x^2} = -2K. \tag{2.2}$$

Due to the cylindrical symmetry of the system, we obtain:

$$\frac{\partial^2\Phi}{\partial y^2} = \frac{\partial^2\Phi}{\partial x^2} = -K. \tag{2.3}$$

Solving these equations leads to:

$$\Phi(x,y,z) = K(z^2 - \frac{1}{2}x^2 - \frac{1}{2}y^2) = K(z^2 - \frac{1}{2}\rho^2) = \Phi(z,\rho), \tag{2.4}$$

where ρ corresponds to the radial distance and is equal to (x^2+y^2). By inserting a constant potential into the above formula the equipotential planes can be calculated. Taking one of these equipotential planes as an electrode, each electrode having a constant potential everywhere, the respective shape of the end electrode and of the ring electrode for the chosen potential is obtained:

$$z^2 = z_0^2 + \frac{1}{2}\rho^2; \quad z^2 = \frac{1}{2}\rho^2 - \frac{1}{2}\rho_0^2, \tag{2.5}$$

z_0 and ρ_0 being the geometrical distances of the trap, measured from the trap center to the surface of the electrode in axial and in radial direction. If one accounts for this and places a potential of $\frac{1}{2}V_0$ on the outer electrodes and a potential of $-\frac{1}{2}V_0$ on the ring electrode in the middle of the trap, the following potential is obtained in the trap:

$$V(z,\rho) = V_0\frac{z^2 - \frac{1}{2}\rho^2}{z_0^2 + \frac{1}{2}\rho_0^2} - \frac{1}{2}V_0\frac{z_0^2 - \frac{1}{2}\rho^2}{z_0^2 + \frac{1}{2}\rho_0^2}. \tag{2.6}$$

Now it is sensible to introduce a new parameter that depends only on the geometry of the trap:

$$d^2 = \frac{1}{2}\left(z_0^2 + \frac{1}{2}\rho_0^2\right). \tag{2.7}$$

Then Equation (2.6) simplifies to

$$V(z,\rho) = \frac{V_0}{2d^2}\left(z^2 - \frac{1}{2}z_0^2 + \frac{1}{4}\rho^2\right). \tag{2.8}$$

The cylindrical Penning trap contains several cylindrical electrodes that are placed in succession, as shown in Figure 2.3. The ring electrodes have different lengths and are placed

Fig. 2.3: Three-dimensional sketch of the UNIC cylindrical Penning trap.

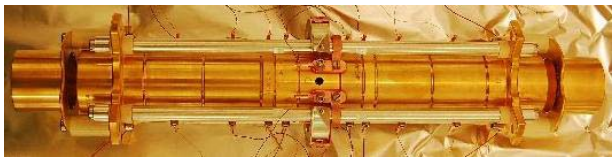

Fig. 2.4: Photograph of the UNIC Penning trap.

at different potentials [22], which results in a three-dimensional potential in the center of the trap. In a cylindrical Penning trap, the end caps have the same cylindrical shape as the ring electrodes, which simplifies the introduction of the ions. Another advantage of the cylindrical Penning trap is the possibility to achieve a greater inner radius so that more ions can be confined. As the creation of multiple neighboring potential wells is possible with the cylindrical Penning trap, differently charged ions can be confined simultaneously. A displacement of the ions by a displacement of the potential could be done with this trap as well, so that the ions in the trap can be brought to every desired position.

The only disadvantage of the cylindrical Penning trap is the potential itself, because it is not quite as harmonic as the potential of a hyperbolical Penning trap. But even the potential of a hyperbolical Penning trap is disrupted by the point of entry of the ions at the endcaps and its size, and the simplicity of the injection of the ions will always compete with the quality of the potential. A calculated potential of a cylindrical Penning trap, which is harmonic in the central region of the trap, can be seen in Figure 2.5. In the course of the ISOLTRAP project at CERN the structure for a cylindrical Penning trap with the best possible harmonic potential for the used number of electrodes has been calculated [22]. It was discovered that the optimal harmonical potential for the seven electrodes used there is achieved by using the voltages and segment lengths given in Table 2.1.

Our Penning trap is inspired by that of ISOLTRAP, the difference being that instead of only seven different potentials we will be using eleven, whereas the four additional potentials are used for trapping the particles, and that our inner radius will be $r_0 = 32$ mm instead of 20 mm. In addition we are using an outer end cap electrode that is divided into only two parts instead of four like it was at ISOLTRAP, and two electrodes have been added on the outside. The inner one can be set to a voltage of 650 V, the outer one to -5 kV which enables the capture of an ion beam with a kinetic energy of 5 keV. The division of the electrodes into two or more parts of the same length permits the abovementioned flexibility so that the plasma can be moved within the trap.

All in all we have discussed two kinds of Penning traps, which are designed such that a harmonic electric field inside the trap can be created. At the lowest point of that field it captures the particles which, by losing energy through synchrotron radiation in the magnetic

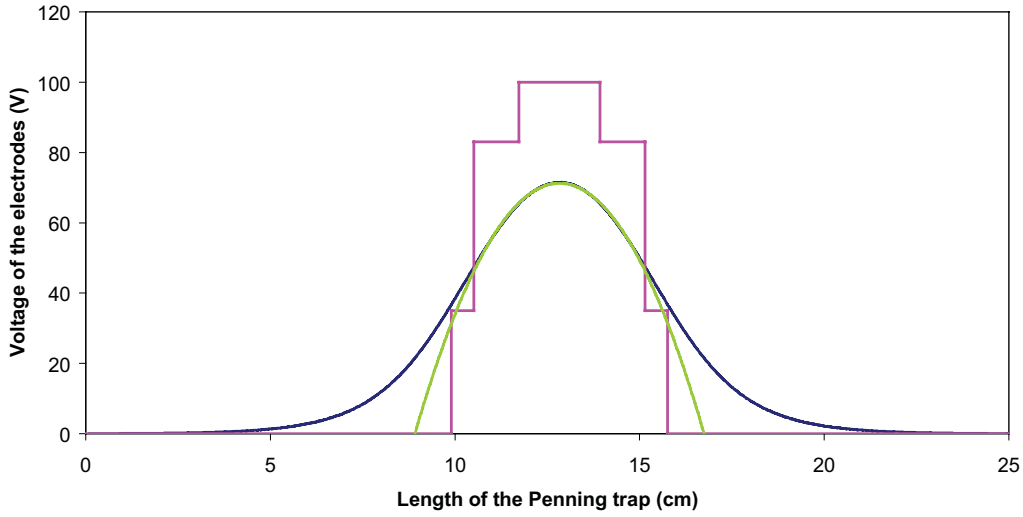

Fig. 2.5: Harmonic potential of our Penning trap on the beam axis with a maximum voltage of 100 V on the ring electrode as shown by the magenta line. There is also a harmonic potential fitted in the trap middle to see how harmonic our cylindrical Penning trap potential will be.

field, have been moving deeper into the potential little by little. Since the synchrotron cooling time scales with the inverse of the particle velocity, and hence the cyclotron frequency, electrons will cool down much faster than heavier particles.

2.2 Aspect ratio α and density

A non-neutral plasma is defined as a collection of charged particles at high density, such that the following condition is satisfied [24]:

$$\lambda_D \ll Z_P, R_P \tag{2.9}$$

where $\lambda_D = \sqrt{(\epsilon_0 k_B T)/(q^2 n)}$ is the Debye length with n the density, q the charge of the particles and Z_P and R_P the elliptical semi-axis of the plasma.

According to a theoretical description based on a cold-fluid model [25] the following equation relates the components of a plasma's dielectric tensor (in Gaussian units):

Tab. 2.1: Optimized lengths l_i and potentials V_i of the electrodes of a cylindrical Penning trap. The lengths are given in units of the inner radius r_0 of the trap elements and the potentials in units of the potential difference between the ring electrode and the outer end cap electrodes [22].

Electrode	V_i/V_0	l_i/r_0
Upper end cap	0	4.00
Upper correction electrode 2	0.34	0.45
Upper correction electrode 1	0.83	0.83
Ring electrode	1.00	1.19
Lower correction electrode 1	0.83	0.83
Lower correction electrode 2	0.34	0.45
Lower end cap	0	4.00

$$\epsilon_3 + m\alpha \left(\alpha^2 - \frac{\epsilon_3}{\epsilon_1}\right)^{1/2} \frac{P_l^m(k_1)}{P_l'^m(k_1)}\,\epsilon_2 = \left(\frac{\alpha^2 - \epsilon_3/\epsilon_1}{\alpha^2 - 1}\right)^{1/2} \frac{P_l^m(k_1)\,Q_l'^m(k_2)}{P_l'^m(k_1)\,Q_l^m(k_2)} \tag{2.10}$$

where α is the aspect ratio Z_P/R_P of the plasma. $P_l^m(k_1)$ and $Q_l^m(k_2)$ are the associated Legendre polynomials with their arguments $k_1 = \alpha\left(\alpha^2 - \epsilon_3/\epsilon_1\right)^{1/2}$ and $k_2 = \alpha\left(\alpha^2 - 1\right)^{-1/2}$. The primes in Equation (2.10) indicate the derivatives, taken with respect to the argument. The ϵ_i are elements of the dielectric tensor that describes a single-component plasma within a homogeneous magnetic field:

$$\begin{bmatrix} \epsilon_1 & -i\epsilon_2 & 0 \\ i\epsilon_2 & \epsilon_1 & 0 \\ 0 & 0 & \epsilon_3 \end{bmatrix}$$

The components of the plasma's dielectric tensor are associated in the following way:

Fig. 2.6: First and second plasma modes, where the first mode is a movement of the complete plasma in z-direction and the second mode a plasma pulsation.

$$\epsilon_1 = \frac{1 - \omega_p^2}{\omega^2 - \Omega_v^2} \tag{2.11}$$

$$\epsilon_2 = \frac{\Omega_v \omega_p^2}{\omega\left(\omega^2 - \Omega_v^2\right)} \tag{2.12}$$

$$\epsilon_3 = \frac{1 - \omega_p^2}{\omega^2} \tag{2.13}$$

with $\omega_p = \left(q^2 n/\epsilon_0 m\right)^{1/2}$ the angular plasma frequency, where m is the mass of the charged particles. ω is the angular frequency of the disturbed potential Ψ from the assumption of a time dependency $e^{i\omega t}$, $\Omega_v = \Omega_c - 2\omega_r$ the vortex frequency with $\Omega_c = qB/mc$ and ω_r the rotation frequency of the cloud which, by $\omega_p^2 = 2\omega_r\left(\Omega_c - \omega_r\right)$, is connected to the plasma frequency.

From Equation (2.10) it can be derived [26] that by measuring only two individual modes, specified by the l's and m's of the associated Legendre polynomials [24], the density and the aspect ratio α can be determined. This will become clear when looking at Equation (2.20) later on. Here only the first two modes, represented in Figure 2.6, are of interest.

The other modes, shown in Figure 2.7, are also ascertainable by the following equations, but are not required, as should become clear when looking at the following formulas. In addition the use of those other modes is rendered more difficult by the fact that their frequencies are too high and the fact that, after they have been artificially generated, they die down too quickly to give enough time for a measurement and those modes do not provide more plasma informations.

The first mode is just a horizontal flow of the plasma cloud along the z-axis, the same direction as that of the electron beam which delivers the electrons for the plasma. For an ideal Penning trap the first mode can be accurately calculated. We can establish the

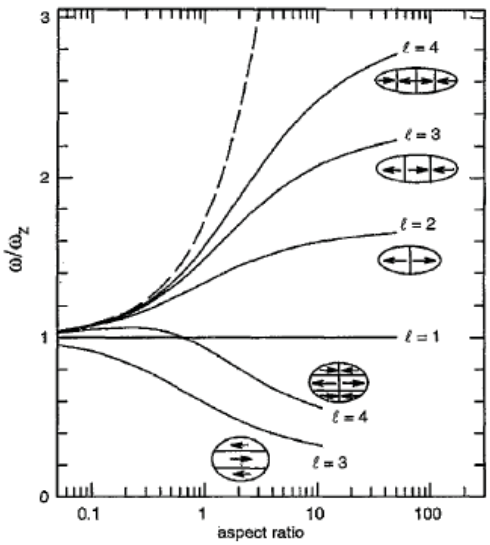

Fig. 2.7: Plasma mode frequency as a function of aspect ratio for several low-order modes, scaled by ω_z. The dashed line is the plasma frequency (Figure taken from [24]).

differential equation for the horizontal motion of the entire plasma cloud and estimate the frequency of the dipole motion:

$$\ddot{z} = \frac{F_z}{m} \tag{2.14}$$

with

$$F_z = q\,E_z = q\frac{\partial V}{\partial z} = \frac{qV_0 z}{d^2} \tag{2.15}$$

it follows:

$$\ddot{z} = -\omega_1^2 z, \tag{2.16}$$

such that we get [21]:

$$\omega_1 = \sqrt{\frac{qV_0}{d^2 m}}. \tag{2.17}$$

But the above derivation of the frequency is not quite valid for our potential because it is not perfectly harmonic, and the geometric factor d is not defined for a cylindrical

Penning trap. But d can be regarded approximately as the distance that the plasma is able to move and we can approximate it by the full width at half maximum of the potential and thereby estimate the frequency of the first mode. But it is not necessary to be able to calculate the exact frequency as we will be able to measure it.

As mentioned above, the frequencies of the other modes can also be calculated. For the relation between the plasma frequency and the frequency of the first mode we have [26]:

$$\omega_p^2 = \omega_1^2 \frac{2}{A_3(\alpha)} \tag{2.18}$$

with

$$A_3(\alpha) = \frac{2Q_1^0\left[\alpha\left(\alpha^2-1\right)^{-1/2}\right]}{\alpha^2-1}, \tag{2.19}$$

where Q_1^0 is again a Legendre polynomial that can this time be solved analytically [24]:

$$\frac{\omega_p^2}{\omega_1^2} = \begin{cases} (1-\alpha^2)^{3/2}\left(\sqrt{1-\alpha^2} - \alpha\cdot\arcsin\sqrt{1-\alpha^2}\right)^{-1}, & \text{for } \alpha < 1, \\ (\alpha^2-1)^{3/2}\left\{(\alpha/2)\ln\left[\frac{\alpha+\sqrt{\alpha^2-1}}{\alpha-\sqrt{\alpha^2-1}}\right] - \sqrt{\alpha^2-1}\right\}^{-1}, & \text{for } \alpha > 1. \end{cases} \tag{2.20}$$

In the case of our trap $\alpha > 1$. For the quadrupole mode frequency, the frequency of the second mode, Tinkle obtains a frequency relative to that of the first mode [24]:

$$\frac{\omega_2^2}{\omega_1^2} = 1 + \frac{\alpha^2}{\alpha^2-1}\frac{(\alpha^2+\frac{1}{2})\ln\left[\frac{\alpha+\sqrt{\alpha^2-1}}{\alpha-\sqrt{\alpha^2-1}}\right] - 3\alpha\sqrt{\alpha^2-1}}{(\frac{\alpha^2}{2})\ln\left[\frac{\alpha+\sqrt{\alpha^2-1}}{\alpha-\sqrt{\alpha^2-1}}\right] - \alpha\sqrt{\alpha^2-1}}. \tag{2.21}$$

This equation is plotted in Figure 2.8. With the help of this formula and the frequency measurements of the first and second mode the corresponding aspect ratio α can be calculated. Unfortunately the solution for α can only be obtained numerically. Using α, the above Equation (2.20) and the first measured frequency, we can now determine the plasma frequency ω_p.

Since the charge and the mass of the ions are known, it is possible to determine the particle density n, if the number of particles in the plasma is also measured. With this measurement their total charge is measured and divided by the known individual charge of each ion. If the particle number of the plasma has been determined, its volume can be found and thereby its geometry. Thus only the frequencies of the first two modes have to be measured to find the aspect ratio α, the density and the radii of the plasma. In our case with an electron plasma confined in an electric potential of some tens of volts the first mode will be found in the interval from 20 to 30 MHz, the second mode in the interval from 40 to 45 MHz.

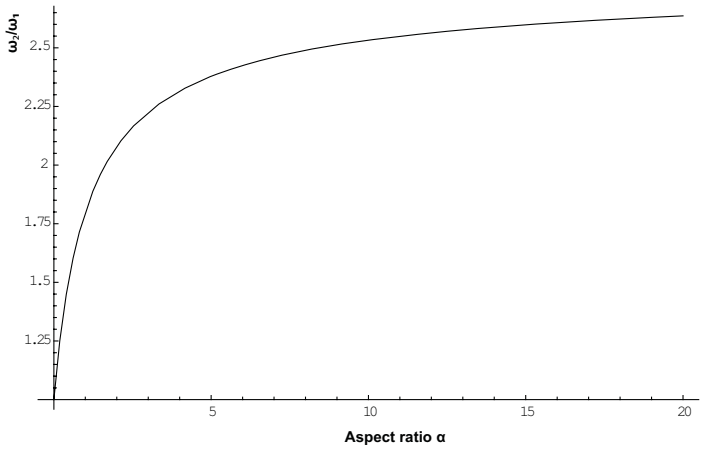

Fig. 2.8: Ratio of the plasma mode frequencies as a function of the aspect ratio α.

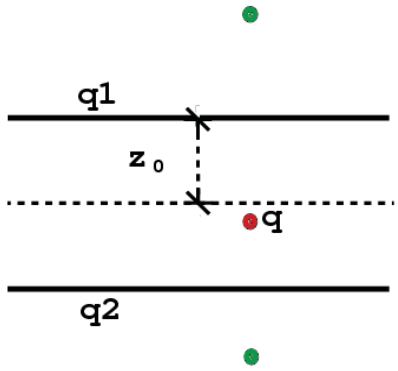

Fig. 2.9: Plate capacitor (Figure taken from [21]).

2.3 Measurement of the plasma mode frequencies

The detection is based on the measurement of the current induced by moving electrons of the plasma on an electrode of the Penning trap. To do this we consider a simple example first: A parallel-plate capacitor as can be seen in Figure 2.9. Positioning a real charge q between the capacitor plates, the induced charges on the plates are given by the following equations [21]:

$$q_1 = -q\frac{z_0 + z}{2z_0}, \quad q_2 = -q\frac{z_0 - z}{2z_0}, \tag{2.22}$$

where z_0 is the distance between the charge and the capacitor plate. We further have:

$$q_1 + q_2 + q = 0. \tag{2.23}$$

For the current I induced between the plates we obtain:

$$I = \frac{\partial q}{\partial t} = -q\frac{\dot{z}}{2z_0}, \tag{2.24}$$

which yields the following expression for the potential if a detection resistance R is connected between the electrodes:

$$\Delta V = RI = -Rq\frac{\dot{z}}{2z_0}. \tag{2.25}$$

A correction factor β has to be added for the Penning trap because of the curvature of its electrodes, which are cylindrical and not plates:

$$\Delta V = -\beta Rq\frac{\dot{z}}{2z_0}. \tag{2.26}$$

An externally excited ion moves according to the differential equation:

$$m\ddot{z}(t) + m\Gamma\dot{z}(t) + m\omega_z^2 z(t) = F_0 \cos(\omega t). \tag{2.27}$$

This is the differential equation of a harmonic oscillator where a damping term with damping constant Γ and a periodically exciting force F_0 have been added. The general solution of the homogeneous differential equation is:

$$z_h(t) = e^{-(1/2)\Gamma t}[A_1 \sin(\omega_l t) + B_1 \cos(\omega_l t)], \tag{2.28}$$

where $\omega_l = \sqrt{\omega_z^2 - (\Gamma)^2}$ is the sought-after frequency and ω_z is the angular frequency of the ordinary differential equation. A particular solution of the inhomogeneous differential equation is:

$$z_p(t) = A \sin(\omega t) + B \cos(\omega t). \tag{2.29}$$

For the relation of the amplitudes we obtain:

$$A_1 = -A = -\frac{F_0}{m}\frac{\Gamma\omega}{\left(\omega_l^2 - \omega^2\right)^2 + \Gamma^2\omega^2} = -A_{abs}, \tag{2.30}$$

$$B_1 = B = \frac{F_0}{m}\frac{\omega_l^2 - \omega^2}{\left(\omega_1^2 - \omega^2\right)^2 + \Gamma^2\omega^2} = A_{el}, \tag{2.31}$$

where A_{abs} should be the absorbed amplitude and A_{el} the elastic amplitude. The complete solution is therefore:

$$z(t) = A_{abs}[\sin(\omega t) - e^{-(1/2)\Gamma t}\sin(\omega_l t)] + A_{el}[\cos(\omega t) - e^{-(1/2)\Gamma t}\cos(\omega_l t)]. \tag{2.32}$$

The two amplitudes have the following relation:

$$\frac{A_{abs}}{A_{el}} = \frac{\omega_l^2 - \omega^2}{\Gamma\omega}. \tag{2.33}$$

Knowing that the exciting force is the electrical force due to the potential applied to the electrodes, its magnitude can be determined from the abovementioned current and the potential in equation (2.26):

$$F_0 = \frac{P}{\dot{z}} = \frac{\Delta V_d I}{\dot{z}} = \frac{\beta q \Delta V_d}{2z_0}, \tag{2.34}$$

where P is the power and V_d is the stimulated "drive" potential. Plugging this into Equation (2.27) we obtain:

$$m\ddot{z}(t) + m\Gamma\dot{z}(t) + m\omega_z^2 z(t) = \frac{\beta q \Delta V_d}{2z_0}\cos(\omega t). \tag{2.35}$$

During the stimulation the attenuation can be neglected, so $\Gamma \approx 0$ and the amplitude A_{abs} vanishes as can be seen from Equation (2.30), such that the solution of the differential equation is modified and now becomes:

$$\begin{aligned} z(t) &= A_{el}[\cos(\omega t) - \cos(\omega_l t)] = \frac{\beta q \Delta V_d}{2z_0 m}\frac{\cos(\omega t) - \cos(\omega_l t)}{\omega_l^2 - \omega^2} \\ &= A_{mod}(t)\sin\left(\frac{\omega_l + \omega}{2}t\right), \end{aligned} \tag{2.36}$$

where

$$A_{mod}(t) = \frac{\beta q \Delta V_d}{2 z_0 m} \frac{2 \sin\left(\frac{\omega_l - \omega}{2} t\right)}{\omega_l^2 - \omega^2} \tag{2.37}$$

is the amplitude during the stimulation. If the stimulation time is much shorter than the inverse of the difference

$$\tau_d \ll \frac{1}{\omega_l - \omega}, \tag{2.38}$$

which can easily be achieved by choosing a stimulation frequency ω that is very close to the sought-after frequency ω_l, the amplitude $A_{mod}(t)$ can be Taylor expanded:

$$A_{mod}(t) \approx \frac{\beta q \Delta V_d}{2 z_0 m} \frac{t}{\omega_l + \omega}. \tag{2.39}$$

For many charged particles like a plasma the following equation for the amplitude is obtained:

$$A_{mod}(t) \approx \frac{\beta q \Delta V_d}{N 2 z_0 m} \frac{t}{\omega_l + \omega}, \tag{2.40}$$

N being the particle number. As one can see, the particle number could also be determined by conducting an amplitude measurement at a known resonance frequency if the geometrical factor β was known. It is possible to calculate this factor, but a measurement with an MCP (multi channel plate detector) is generally more reliable.

As soon as the stimulation comes to an end, the plasma oscillates freely. This process of stimulation and following free oscillation can be seen in Figure 2.10. During free oscillation the damping term introduced above appears:

$$z(t) = A_{mod}(\tau_d) e^{-\frac{1}{2}\Gamma t} \sin\left(\omega_l t + \phi\right). \tag{2.41}$$

The amplitude A_{mod} is simply the value at the end of the stimulation time τ_d. ϕ is a phase and ω_l the frequency that is to be measured. Plugging this expression into Equation (2.26) the potential is expressed by:

$$V_{plas}(t) = -\beta R q \frac{\dot{z}}{2 z_0}. \tag{2.42}$$

Differentiating $z(t)$ with respect to time t results in the following:

$$\dot{z}(t) = A_{mod}(\tau_d) e^{-\frac{1}{2}\Gamma t} \left(-\frac{1}{2}\Gamma \sin\left(\omega_l t + \phi\right) + \omega_l \cos\left(\omega_l t + \phi\right) \right). \tag{2.43}$$

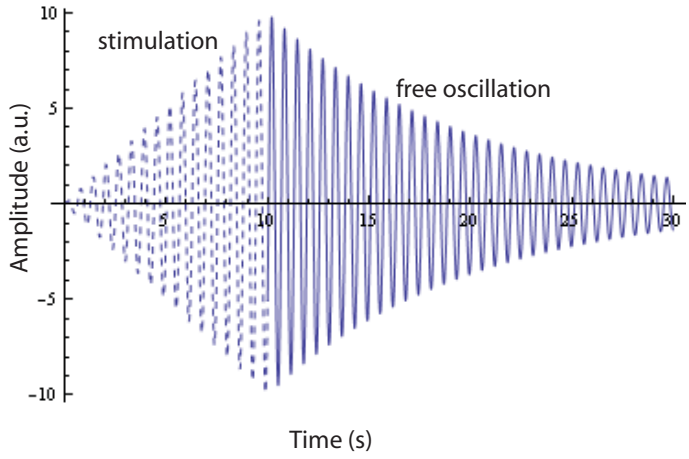

Fig. 2.10: Stimulation followed by free oscillation of the plasma.

Earlier measurements by ATHENA have shown that the full width at half maximum $\tau = 1/\Gamma$ is about 30 µs which corresponds to a frequency of about 33 kHz. It is further known that the sought-after frequencies of the plasma modes are situated in the interval from 20 to 60 MHz. This means that ω_l is about four orders of magnitude greater than Γ, so that the first summand in the brackets can be neglected. Combining the time-dependent terms and some parameters in a function $A(t)$ the following equation is obtained [27]:

$$V_{plas}(t) \propto \omega_l A(t) \cdot \cos(\omega_l t + \phi). \tag{2.44}$$

Afterwards the potential is multiplied by a sine and a cosine to create sidebands and simplify data storage:

$$I_m(t) = V_{plas}(t) \cdot \sin(\omega_d t), \tag{2.45}$$
$$Q_m(t) = V_{plas}(t) \cdot \cos(\omega_d t), \tag{2.46}$$

where $I_m(t)$ is an in-phase function and $Q_m(t)$ a function shifted by 90° (quadratic). Supposing that the stimulation frequency is close to the frequency of the measured mode, the addition formulas for the sine and the cosine can be used and one obtains:

$$I_m(t) \propto \omega_l A(t) \left\{\sin\left[(\omega_l - \omega_d)t + \phi\right] + \sin\left[(\omega_l + \omega_d)t + \phi\right]\right\}, \tag{2.47}$$
$$Q_m(t) \propto \omega_l A(t) \left\{\cos\left[(\omega_l - \omega_d)t + \phi\right] + \cos\left[(\omega_l + \omega_d)t + \phi\right]\right\}. \tag{2.48}$$

The difference of the frequencies is a very low frequency that is measurable, while the sum of the frequencies is a high frequency that can easily be removed with a low-pass filter.

The following two signals are the ones remaining after the hardware filter:

$$I(t) \propto \omega_l A(t) \sin\left[(\omega_l - \omega_d)t + \phi\right], \tag{2.49}$$
$$Q(t) \propto \omega_l A(t) \cos\left[(\omega_l - \omega_d)t + \phi\right]. \tag{2.50}$$

Using simple trigonometrical operations we get:

$$\omega_{lk} - \omega_d = \left[\arctan\left(\frac{I_{k+1}}{Q_{k+1}}\right) - \arctan\left(\frac{I_k}{Q_k}\right)\right] \cdot \frac{1}{T_s}. \tag{2.51}$$

The k represent different measured data points following a single stimulation. The time T_s is the time between consecutive measurements. Since the stimulation frequency is known, it is possible to calculate the sought-after frequency of the stimulated plasma mode. To keep the uncertainty as small as possible, the mean of all measured plasma frequencies ω_l is taken. The whole measurement process is summarized in the flowchart shown in Figure 2.11.

2.4 Rotating wall

The rotating-wall technique is a method used to compress or expand a plasma in a Penning trap. By means of an electric dipole field that rotates around the z axis. To create such a rotating electric dipole field, a four segmented ring electrode is used, which can be seen in Figure 2.12. Sinusoidal voltages U_d, applied to the four segments with their relative phases shifted by 90° between consecutive segments, produce a time-dependent potential that is superimposed on the trapping potentials. For these four phase-shifted voltages a special generator is used. In spite of this additional potential the axial component of the plasma motion remains unaffected.

To understand how the applied electric dipole field influences the plasma, we have to understand the correlation between the plasma rotation frequency and the plasma density. In equilibrium for a single charged particle with mass m that rotates with the frequency ω the Lorentz force equals the sum of the Coulomb and centripetal forces [28]:

$$q\omega r B = m\omega^2 r + \frac{nq^2 r}{2\epsilon_0}, \tag{2.52}$$

where n is the ion density and ϵ_0 the vacuum permittivity.

We then obtain a quadratic equation for the rotation frequency for a plasma:

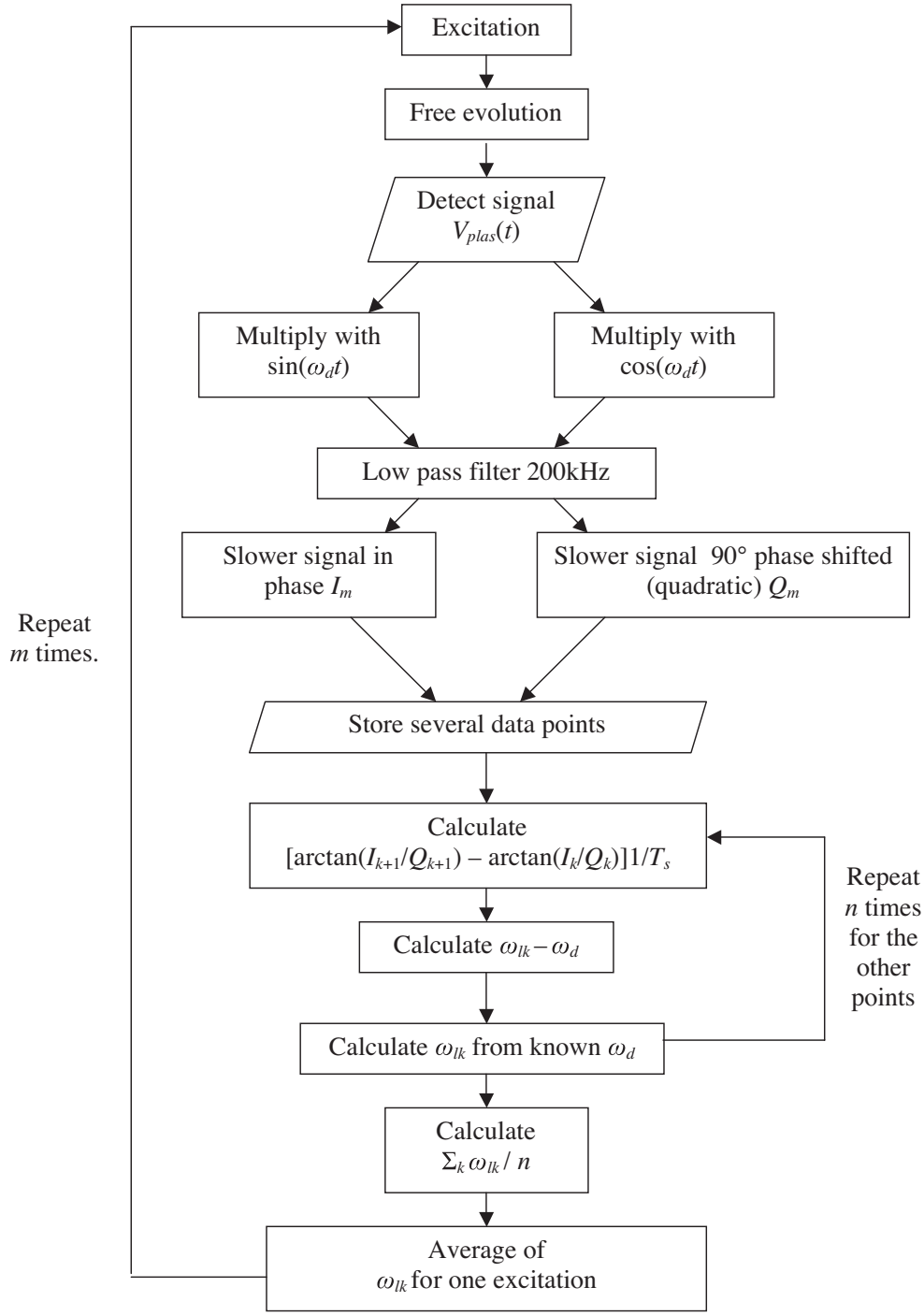

Fig. 2.11: Flowchart of the entire measurement process of the plasma mode frequencies. One excitation takes 200 kHz. So 5 excitations per mode are needed for a frequency sampling of 1 MHz.

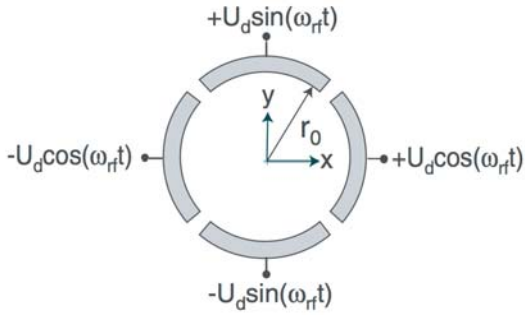

Fig. 2.12: Creation of a rotating dipole field around the z axis (Figure taken from [28]).

$$\omega\omega_c = \omega^2 + \frac{\omega_p^2}{2}. \tag{2.53}$$

The solutions for ω are [28]:

$$\omega_\pm = \frac{1}{2}\left(\omega_c \pm \sqrt{\omega_c^2 - 2\omega_p^2}\right). \tag{2.54}$$

The plot of this solution can be seen in Figure 2.13 in units of ω_c as a function of the density n/n_B. The two solutions for the rotation frequency ω yield the same value for

$$\omega_p^2 = \frac{1}{2}\omega_c. \tag{2.55}$$

At this value both the plasma frequency and the density n reach their maximum values:

$$n_B = \frac{\epsilon_0 B^2}{2m}. \tag{2.56}$$

This value is called Brillouin limit and only depends on the magnetic trap field and the ion mass. At maximal plasma density the rotation frequency becomes

$$\omega = \frac{1}{2}\omega_c. \tag{2.57}$$

In Figure 2.13 it can be seen that an increase of the rotation frequency ω_- leads to an increase of the density n if the plasma rotation frequency ω is smaller than $\omega_c/2$. And because of low ion densities and high magnetic fields and therefore a high ω_c, this is the case in most Penning traps.

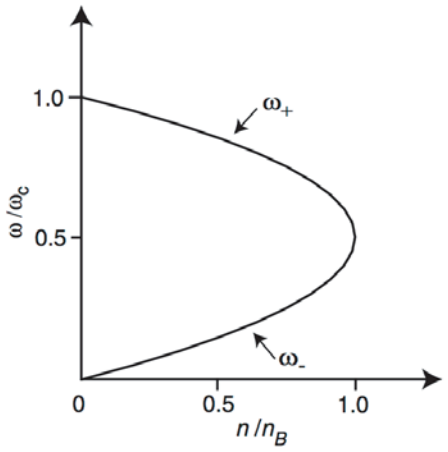

Fig. 2.13: Correlation between the rotation frequency ω of a confined plasma in a Penning trap in thermal equilibrium, normalized to the cyclotron frequency ω_c and the plasma density n, normalized to the Brillouin limit n_B (Figure taken from [28]).

The rotating fields transfer angular momentum to the ions. For a trapped plasma the torque affects the outer particles first. Due to the Coulomb interaction between the ions the torque is transferred to the whole plasma, and the plasma spheroid is accelerated. Thereby the radially inward Lorentz force, caused by the movement of the ions in the magnetic field, is increased. If this Lorentz force is larger than the sum of the Coulomb and centripetal forces, the plasma's radial extension decreases and the plasma is compressed.

3. ELECTRON GUN AND SOURCE

3.1 Requirements of the electron gun

Several requirements had to be met in the design and construction of the electron gun:

1) The position of the source is crucial. Hence the electron gun should not be fixed at its position, but be movable by means of an x-y-z manipulator to enable rectifying any deviations from the trap center later on.

2) Further, the distance to the trap and therefore to the magnetic field is important as well, because the closer the electron gun is to the trap the simpler it becomes to guide the electrons into the trap. But the distance to the trap is for the most part fixed by the geometry of the apparatus.

3) Another requirement is that the BaO electron source should be easily removable from the electron gun, because the source only has a limited lifetime and must be replaced from time to time. Essentially the BaO source consists of a BaO disk that is heated to overcome the work function of the electrons from the BaO.

4) A further criterion is that the electron gun can be rapidly extracted from the axis of the beamline, such that the ions can pass to the trap. This demand has been satisfied by a linear feedthrough which can be retracted and extended pneumatically.

5) Finally the function of the gun is to collimate the emitted electrons to a beam, so that ideally a parallel electron beam leaves the electron gun and reaches the Penning trap.

3.2 Ion-optical simulations

In order not to have to build many electron source prototypes, different designs were simulated first and thereby tested virtually by means of the Simion software. Simion calculates electric and magnetic fields numerically using the relaxation method. Trajectories of ions can also be calculated by Simion with numerical (Runge-Kutta) integration, an iterative method. With these trajectory calculations, three effects can be accounted for: Electric and magnetic deviation as well as charge repulsion. In the present calculations, however, only

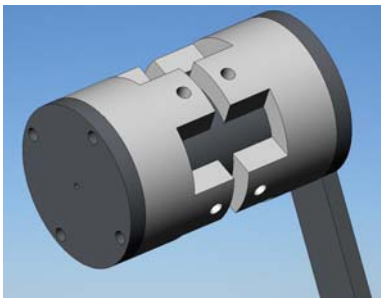

Fig. 3.1: First try for the electron gun (front).

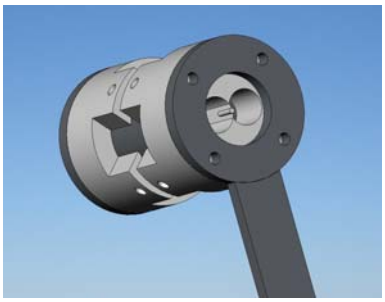

Fig. 3.2: First try for the electron gun (back).

the electric deviation and the charge repulsion were considered. With any change in the electrode geometry, the potentials of the individual electrodes have to be recalculated and they may have to be redesigned with SolidWorks and reimported to Simion.

However, a change in the length of the main cylindrical electrode could be directly simulated by displacing the starting point of the electrons in relation to the position of the cylinder.

3.3 The different designs

As a starting point for further improvements, the design shown in Figures 3.1 and 3.2 was chosen. This first sketch consists of only six components: The electron gun itself, the fastener which attaches the electron source to the linear feedthrough, two PEEK insulators, a cylinder and a front aperture which bundles the electrons and should make sure that they are accelerated towards the Penning trap.

But this first try suffered from the following shortcomings: On the one hand there were potentially many virtual leaks between the PEEK material and that of the cylinder, and on the other hand the source on the inside was not attached optimally because the PEEK material was connected to the cylinder with screws going in radial direction. This way the force which is induced by the screws acts in radial direction as well instead of along the symmetry axis. A small variation in the manufacturing of the source could thereby generate a slight shift that would be fatal for its effectiveness. In addition the sketch incorporated some unnecessarily complicated manufacturing. The electron gun was redesigned based on these points and the result can be seen in Figures 3.3 and 3.4.

In the next iteration, the design was kept quite simple. There was a support that pressed the electron source on the cylinder. The cylinder itself was kept at a negative potential to focus the electrons and finally accelerate them. Additionally there was the grounded

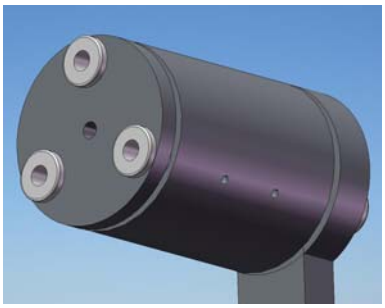

Fig. 3.3: Second try for the electron gun (front).

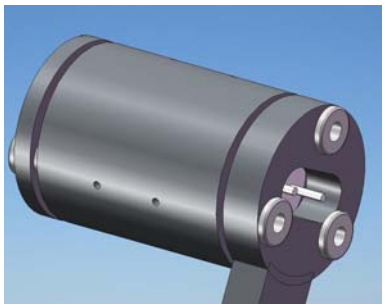

Fig. 3.4: Second try for the electron gun (back).

aperture in front of the cylinder, in order to create an electric field between the cylinder and the aperture and accelerate the electrons towards the aperture. A simulation of this design was performed, analyzing mainly the emission and the divergence of the electrons. The key quantity was the number of electrons arriving on a disk that was situated at a distance equal to the distance between the Penning trap and the electron source. There were a few other parameters that were tested, of which the only one of importance was the length of the cylinder. The result of this design in terms of its efficiency can be seen in Figure 3.5. As is plainly visible the largest electron output is obtained at a cylinder length of 13.5 cm. Next, the potential of the cylinder was chosen as variable parameter while the cylinder length was kept constant. The result of these parameter optimizations is shown in Figure 3.6. The latter case were scanned in smaller increments to enable a more accurate determination of the peak.

Figure 3.7 answers the question why there was a maximum output at this cylinder length. The lines represent the electron current of the electron gun. Looking at the first pane it is obvious that the starting point for the electrons, lying in the cylinder, is too far back. This example is similar to that of an infinitely long cylinder which has no electric field inside. The emitted electrons do not "see" the electric field and are not accelerated. Only a few of the electrons diffuse far enough to arrive at a point where the electric field starts acting on them. They descend the potential slope and are accelerated. The second figure represents the ideal case. In this position, the greatest intensity was achieved. The electrons start at the edge of the highest point of the electrical potential and so all are accelerated towards the front. The third figure shows what happens when the electron source is situated too far towards the front. In this scenario, the electrons only feel a weak electric field and are not collimated and accelerated correctly. The divergence of the electron beam is consequently increased, for without acceleration there is no preferential direction. Only very few electrons will reach the trap.

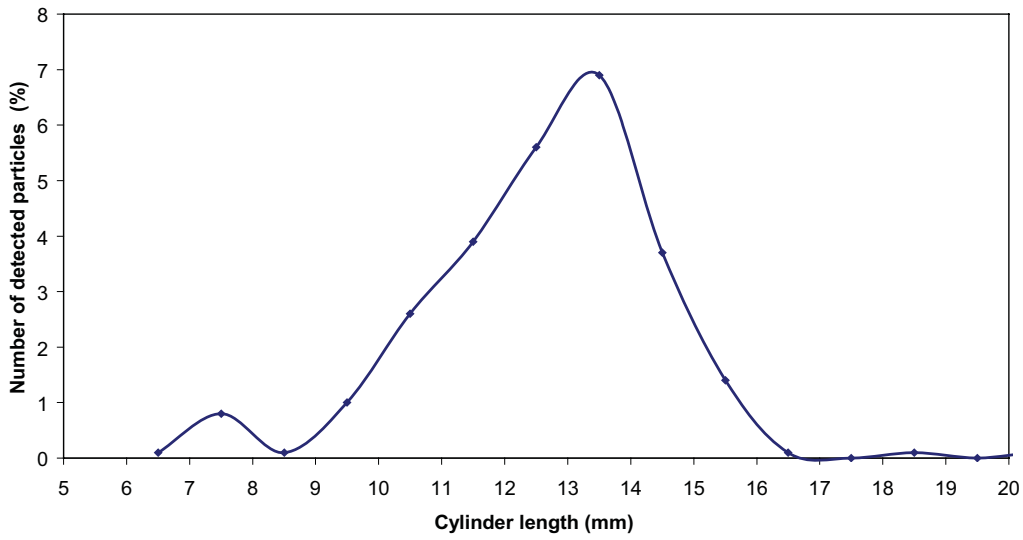

Fig. 3.5: Efficiency as a function of cylinder length with a cylinder voltage of 50 V and an aperture voltage of 0 V.

The result of 14% of the electrons reaching the trap with this configuration was not at all satisfying. Once the right cylinder length had been found, the electron beam was still far too divergent and had to be collimated. Several different aperture designs were tested, but at some point the geometric enhancement of the aperture was given up and the attention was turned to altering the design of the electron gun more radically. The new design aimed for a better collimation of the electrons, the poor collimation being the reason the first tests failed. The electron gun was now combined with two apertures, which acted as collimating lenses. The design can be seen in Figures 3.8 and 3.9. The result of the simulation can be seen in Figure 3.10 A). Here a slight increase of efficiency can be noted. Unfortunately this design brings with it an increase in the number of free parameters: Three parameters for the distances of the apertures, one for the voltage of the cylinder and the collimating aperture, another for the position of the electron source in the cylinder, three for the thickness of the apertures and another three for the size of the aperture holes. All in all the number of parameters was up to twelve, all of them correlated. These parameters were now iteratively modified and ion trajectories simulated until the result in Figure 3.10 B) was achieved.

With an aperture voltage of 55 V, a cylinder voltage of 100 V and the indicated parameters the efficiency reached 99.2%. The remaining electrons deviated from the desired path because they had been emitted in the opposite direction due to statistical fluctuations in

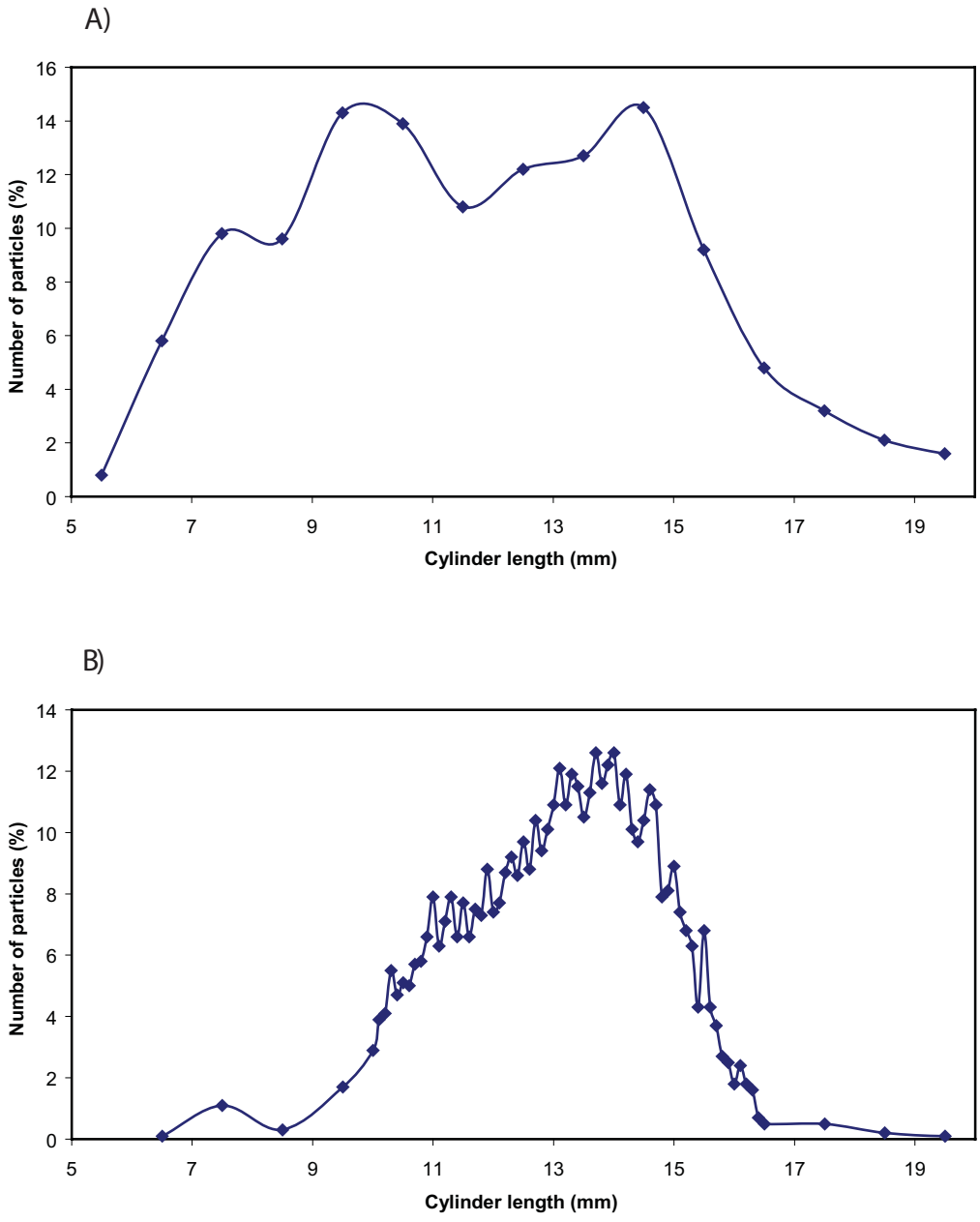

Fig. 3.6: Efficiency as a function of cylinder length with A) a cylinder voltage of 150 V and an aperture voltage of 0 V, B) a cylinder voltage of 100 V and an aperture voltage of 0 V.

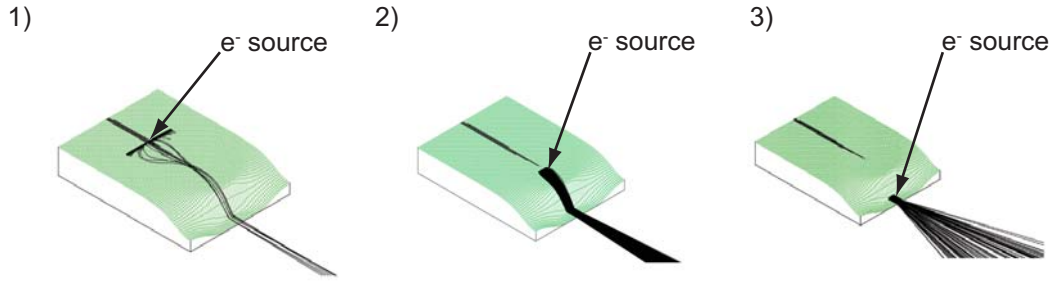

Fig. 3.7: Three different positions for the starting point of the electron source.

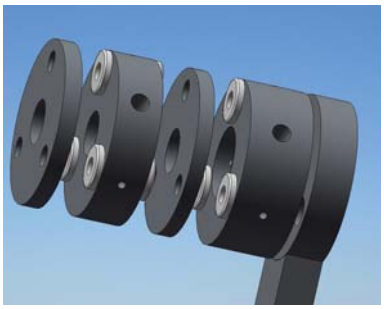

Fig. 3.8: Final version of the electron gun (front).

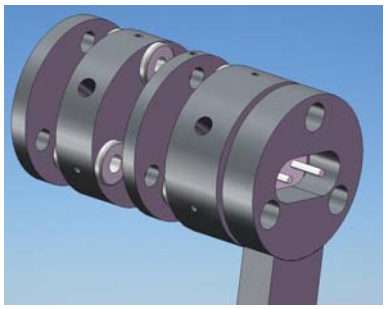

Fig. 3.9: Final version of the electron gun (back).

the start energy that had been included in the simulation.

Finally the decision was made to use the design that showed the maximum efficiency of close to 100%. An additional advantage was the fact that the electrons had been detected at the correct distance in the Penning trap on a disk whose diameter corresponded to that of the electron gun and not the larger diameter of the Penning trap. The application of a magnetic field should further simplify the capture of the electrons into the Penning trap, as the electrons would move in diminishing spirals about the lines of magnetic flux.

3.4 Performance measurements

It was found that the real electron gun behaves a little differently from the simulation. One of the greatest problems was that of optimally adjusting the position of the electron gun, which should be done by observing electrons that are shot through the Penning trap

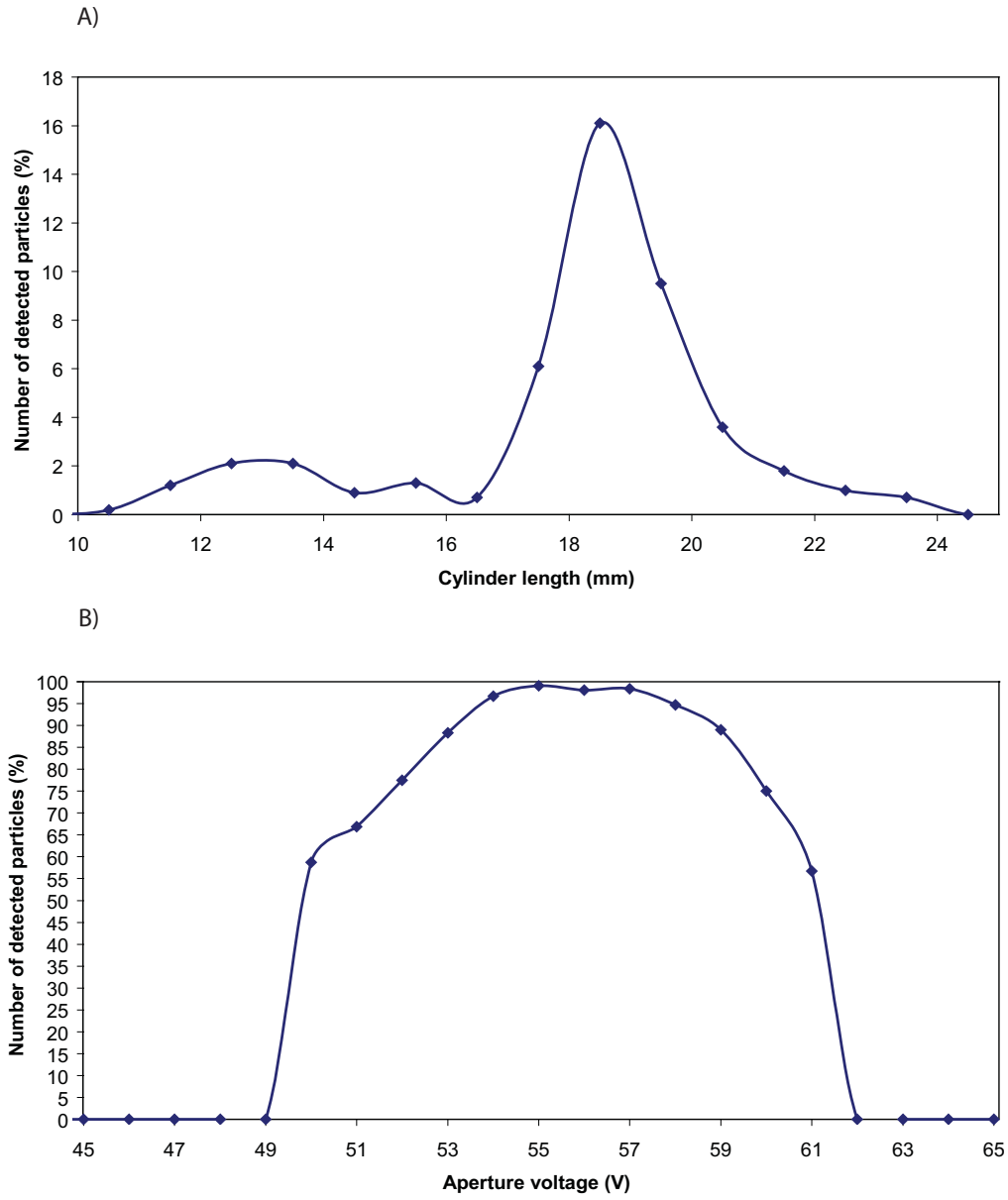

Fig. 3.10: Final version: A) Efficiency as a function of length for a cylinder voltage of 100 V and aperture voltages of 0 V, 75 V and 0 V, B) Efficiency as a function of aperture voltage for a cylinder voltage of 100 V.

on a Faraday cup installed behind the trap. Because the magnetic field tends to focus the electrons through the trap, the shoot-through had to be done with the magnetic field switched off. This, however, did not work at all, hence it was assumed that the electron gun was positioned at an angle with respect to the magnetic-field axis, because a displacement of the electron gun in all three dimensions through the x-y-z manipulator did not lead to a successful transmission. The design was then slightly modified, such that a mirror can be placed in front of the first lens of the gun and small angles can be corrected. A target was then attached in the opening of the Penning trap towards the side of the electron gun and finally the gun was perfectly aligned with the help of a laser beam going through the middle of the Faraday cup and through the target onto the mirror until the laser beam was reflected exactly onto itself. Now, from the perspective of alignment, a shoot-through should have been possible, but still it did not work. The reason for that lay, as calculations revealed, in the Earth's magnetic field.

For the motion of an electron in a magnetic field, the following equation applies:

$$e\, v \times B = \frac{mv^2}{r}. \tag{3.1}$$

So for the radius of the electrons in the magnetic field of the Earth we have $r \approx 0,674$ m for electrons with an initial kinetic energy of 100 eV. They can therefore not reach the Faraday cup at the end of the Penning trap, at a distance of about 80 cm, which explains why none of the electrons arrived there with the solenoidal magnetic field switched off. Through experimenting it was found that a magnetic field of 0.1 T to 0.2 T was sufficient to have the electrons follow the magnetic field without being greatly deflected by the magnetic field of the earth.

Another difference to the simulation is that the same voltage that is applied to the cylinder surrounding the electron source, has to be set on the electron source as well, in order to have them on the same potential. If this is not done, the electron source will be grounded due to its power supply. This was automatically done in Simion because in the simulation there is no necessity of a link between the electron starting point and a power supply unit to obtain the electrons. This is why the graph shown in Figure 3.11 is obtained for a magnetic field of 0.1 T for the correct cylinder voltage. Here it is found that the best efficiency is achieved at about 108 V cylinder voltage. This compares favorably with the design value of 100 V, as seen in Figures 3.5 and 3.6. Next the lens voltage was scanned, as shown in Figure 3.12, at a magnetic field of 0.2 T. As is plainly visible the maximum is at about 50 V which is in agreement with the simulated data, as can be seen in Figure 3.10.

All in all the real values concur quite nicely with the values of the simulation for weak magnetic fields. For strong magnetic fields the voltages of the cylinder and the lens are of lesser importance because the electrons just follow the magnetic field lines. A good example for the fact that the lens voltage does not retain much influence at a magnetic field of 3 T is shown in Figure 3.13. Here one can see that the number of electrons arriving at the

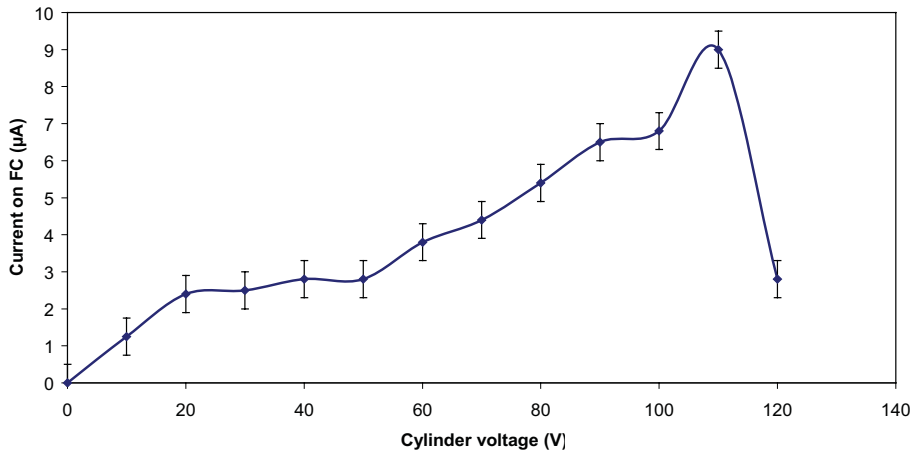

Fig. 3.11: Electron current recorded on the Faraday cup as a function of voltage applied to the cylinder arround the source.

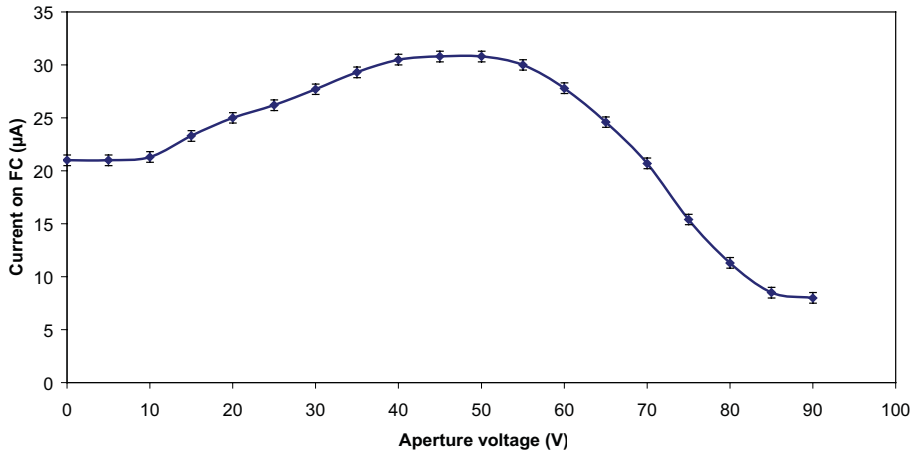

Fig. 3.12: Electron current recorded on the Faraday cup as a function of the voltage applied to the aperture.

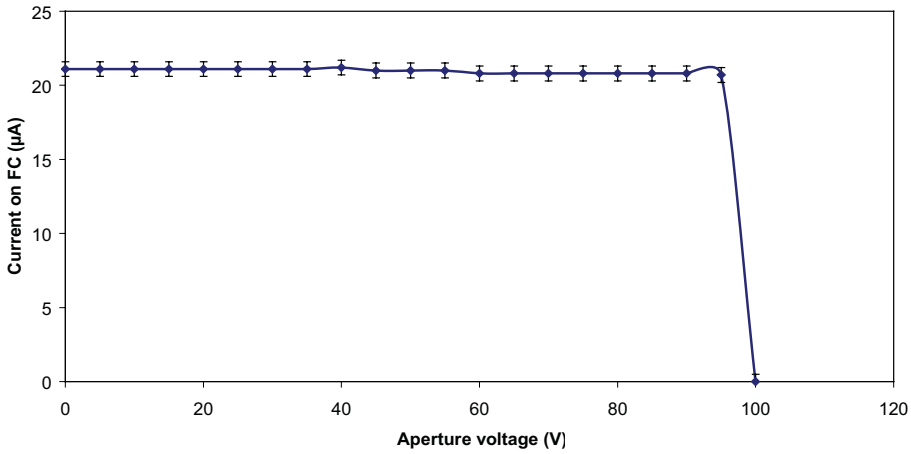

Fig. 3.13: Electron current recorded on the Faraday cup as a function of the voltage applied to the aperture at a 3 T magnetic field.

Faraday cup is almost constant and therefore independent from the lens voltage. At 100 V the number of arriving electrons goes rapidly to zero as the lens acts as a barrier and could actually be used as a switch.

Finally the efficiency of the electron gun was examined. For this purpose, the current that flows from ground into the heating circuit of the electron source was measured as well as the current that arrives at the Faraday cup. The ratio of these currents is shown in Figure 3.14 as a function of the magnetic field.

The figure shows that the efficiency increases with an increasing magnetic field until it reaches 100%. The indicated uncertainty is calculated from the voltmeter reading uncertainty. Some of the values are above 100%. This is due to the offset that was measured at the beginning and then added to each value of the measurement, but unfortunately seems to have changed a little bit during the measurement. The blue line shows the current with the cylinder and aperture voltages set to the optimal values, the magenta line the current with both set to 0 V. The figure shows that the ion-optical elements considerably increase the transmission at low magnetic fields.

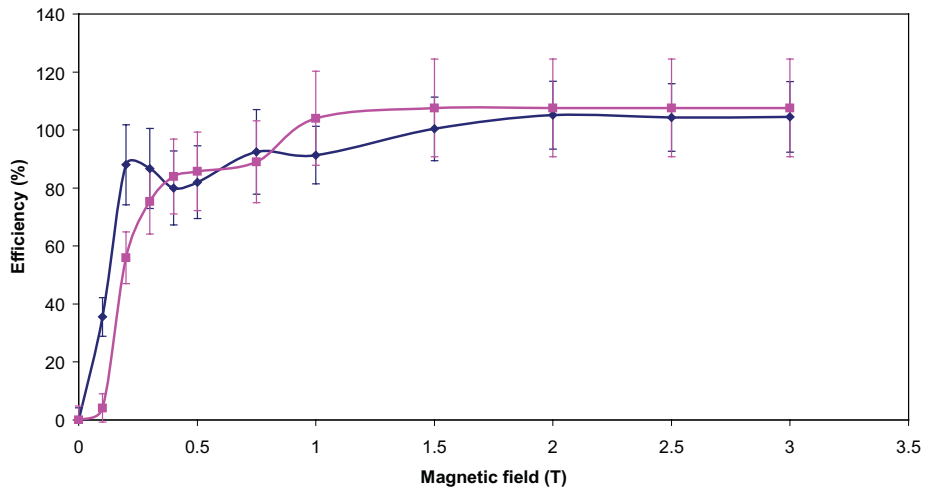

Fig. 3.14: Measured transmission efficiency through the Penning trap as a function of the axial magnetic field. The blue line shows the current with the cylinder and aperture voltages set to the optimal values, the magenta line the current with both set to 0 V.

4. PLASMA LOADING AND DIAGNOSTICS

4.1 Loading of electrons into the Penning trap

In order to create an electron plasma, the electrons have to be loaded into the Penning trap, where they are stopped and confined by the electric and magnetic fields. There are several procedures for the trapping of electrons in the Penning trap. A positive electric potential has to be created by applying voltages to the 13 different trap electrodes, as shown in Figure 2.3. This way many different potentials for ion confinement can be created. The most important of these trapping procedures will briefly be presented here. All trapping tests were executed with a magnetic field of 3.5 T.

First it was tested how many electrons could be caught if, while shooting in the electrons, the outer electrodes were set to -300 V, the second outer electrodes were grounded and the remaining nine electrodes set to a positive potential of $+100$ V, so that the resulting potential is rectangular. As has already been mentioned, electrons emit synchrotron radiation in a magnetic field, thereby lose energy and collect in the axial position of the highest positive potential. After a short time the rectangular potential was changed into a harmonic potential with a voltage of 100 V on the ring electrode because plasma measurements can only be carried out with a harmonic potential. The result was a number of trapped particles of 8×10^6, as measured with the plasma modes diagnostics system based on a calibration performed in Genoa. It was not possible to check this calibration with our apparatus because a micro-channel-plate detector required for this calibration was not yet installed. Therefore, the particle numbers given in this thesis are not absolute and can only be compared to other numbers from our experiment. However, for a determination of the optimal loading procedure, only relative particle numbers are required.

Next we tried the same procedure again, only this time the harmonic potential was created with just the ring electrode on 85 V and therefore the potential was not as deep any more. This procedure did not work at all, which was probably due to the fact that the electrons were already deep in the trap and the 85 V created such a low trap that the electrons were lost during the change from the 100 V rectangular potential to the harmonic potential.

Afterwards we tried to capture the electrons with a triangular potential for which, as above, the outer electrodes were set to -300 V and only the ring electrode to 100 V, while all the other electrodes were grounded. After this the triangular potential was changed to

a harmonic potential, at first with a ring electrode voltage of 100 V, resulting in 4.7×10^6 captured particles, then with a ring electrode voltage of 85 V, resulting in 4.0×10^6 captured particles. Then we tried wider triangular potentials with a voltage of 85 V on the ring electrode. At first the three central electrodes were used to obtain a triangular potential and 7.5×10^6 particles were captured. Then the five center electrodes were used and 7.0×10^6 particles were captured.

Suspecting that some electrons might be lost at the edges of the trap during the reflection process, we tried different trapping procedures with potentials, moving from the trap edges to the middle. Moving triangular potentials were used, each with a depth of 100 V on the electrode at the tip of the triangle and again end electrodes with a potential of −300 V. We let a potential wander from the outer electrode, furthest from the electron gun, to the middle of the trap and there changed it into a harmonic potential with a depth of 100 V on the ring electrode. In this case no electrons were detected. In a second try we let a triangular potential wander from the outer electrode on the other side next to the electron gun to the middle and there become harmonic as well. In this second scenario 7.9×10^6 electrons were detected. The difference between these two scenarios could be due to such a strong reflection of the electrons at the first electrode that they are reflected over the triangle potential of the first scenario. Thereby they can not land in it and are simply lost in the trap while the triangle potential on the other side of the trap seems to collect the reflected particles. Then we tested what happens when both triangle potentials are simultanely created, converge in the middle and become harmonic only afterwards. Doing this we were able to catch 6.5×10^6 particles.

Then we tested a trapping procedure which allows to guide the electrons step by step from the potentials where they are reflected to the deepest potential. The outer electrodes were set to −300 V and from the electrode furthest from the electron gun, a step potential was realized with equidistant steps so that the last step corresponds to a potential created by an electrode set to 100 V. Afterwards the steps were gradually turned into a harmonic potential in the middle of the trap created with the ring electrode at 100 V. Thus 6.6×10^6 particles were captured. Next, a rectangular potential was used and gradually changed to a harmonic potential with a ring electrode at 100 V. Doing this we obtained 8.4×10^6 trapped particles.

Finally the trapping with harmonic potentials from the beginning was tested with differently deep potentials. In order that the outer potentials, up to now always set to −300 V, not disturb the harmonic potential, their voltage was varied as a function of the potential on the outer electrodes. The results are shown in Figure 4.1, where the potentials of the ring electrode are represented as parameters and the potentials of the end electrodes as functions.

Alltogether we achieved the best result by directly loading a harmonic potential which was as deep as possible for our used voltages up to 100 V, while the end caps needed a potential of at least −100 V in order to be able stop the electrons. This also is clearly

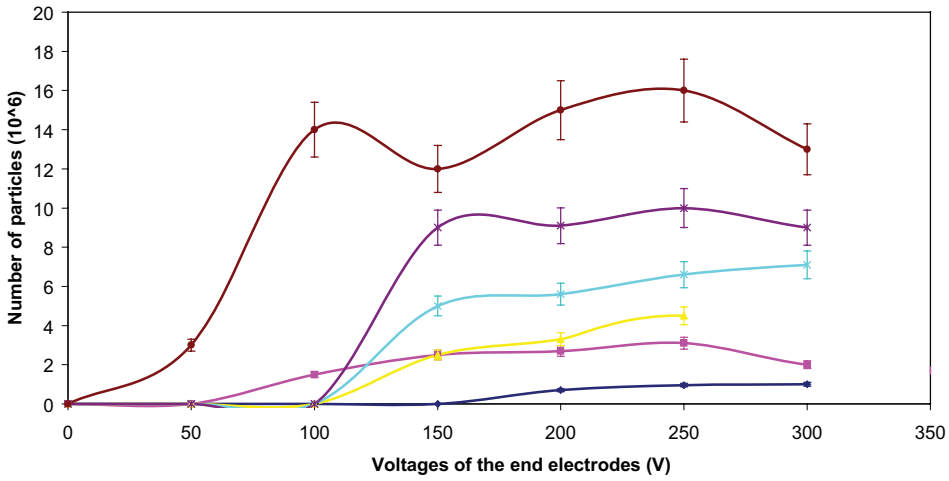

Fig. 4.1: Number of captured electrons as a function of the voltages at the end electrodes. Each curve corresponds to a different potential on the ring electrode: 75 V (dark blue), 80 V (magenta), 85 V (yellow), 90 V (light blue), 95 V (purple), 100 V (brown). The uncertainties originate from a calibration that was done with the mode analyzer used in Genoa.

visible in Figure 4.2 which shows the maximal number of trapped particles depending on the depth of the potential.

If at first anharmonic potentials are used and later turned harmonic, electrons are lost each time the potential is modified. This was verified by several test measurements during which we began with a harmonic potential changed to a rectangular potential and then back to a harmonic one. Each of these changes induced a loss of particles.

4.2 First plasma mode measurements

As has been mentioned in Chapter 2, only the first and the second modes are required for a measurement of the plasma parameters. A typical frequency spectrum of these two modes is shown in Figure 4.3. As is clearly visible, the first mode is at about 25 MHz and the second one at about 40.5 MHz for the chosen trap potential. From these two frequencies the aspect ratio α can be determined by solving Equation (2.21).

The aspect ratio is calculated and displayed in the Labview program. The program will further provide the density, the number of particles and the two radii, as explained in Chapter 2. To accurately display the number of particles and the radii, however, it would

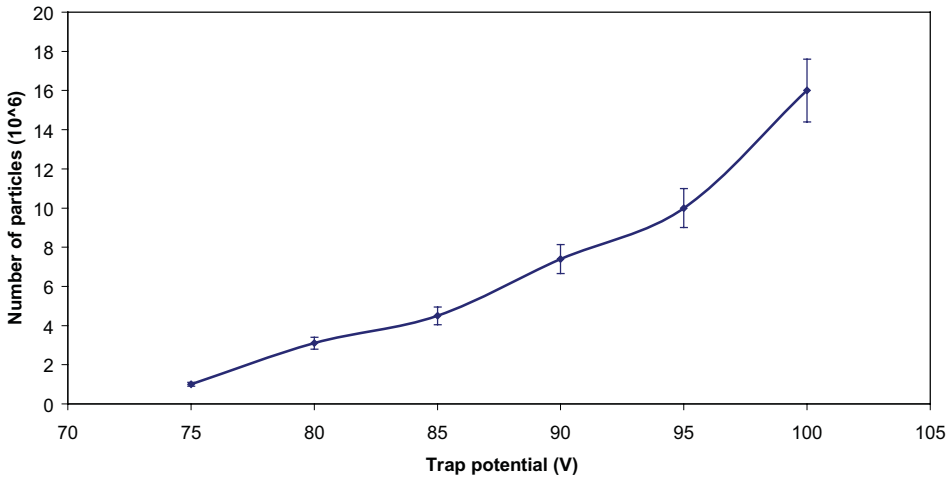

Fig. 4.2: Maximum number of trapped particles as a function of the trap potential. The estimated uncertainty of 10% is due to the calibration of the particle number.

be necessary to determine the number of particles once beforehand and thereby obtain the geometrical factor β in Equation (2.40). Afterwards, the number of particles and the radii will henceforth be calculated and shown correctly.

Absent this calibration, a simpler method of determining α is used in the Labview program. Only the maximum value of the plasma response is taken for each mode and no fit is done. Using the abovementioned Equation (2.21) the aspect ratio α is calculated from these frequencies. In order to double-check the algorithms used by the Labview program, the mode frequencies were manually extracted for one data set. The uncertainties of 10% of the measured values had been determined at the manufacture of the mode analyzer in Genoa by providing a sinusoidal oscillation and then measuring it with the mode analyzer. The result of our fits can be seen in Figures 4.4 and 4.5.

For this purpose, both plasma mode response peaks were fitted with a Gaussian function. In this way, a frequency of 25.0334(24) MHz for the first peak and one of 40.4209(21) MHz for the second peak were obtained. The uncertainties are the standard uncertainties of the fit. The method of only taking the maximum value is sufficient, since it only deviates by at most 0.2% from the fitted graphs. The numerical calculation of the aspect ratio α, according to Equation (2.21), was verified with the help of Mathematica. A relative uncertainty of 10% was assumed. With the values from the fit an aspect ratio α of 15.52 was obtained, which displays only a small deviation from the Labview value of 15.53. Finally the aspect ratio α was again recalculated with a self written C++ program

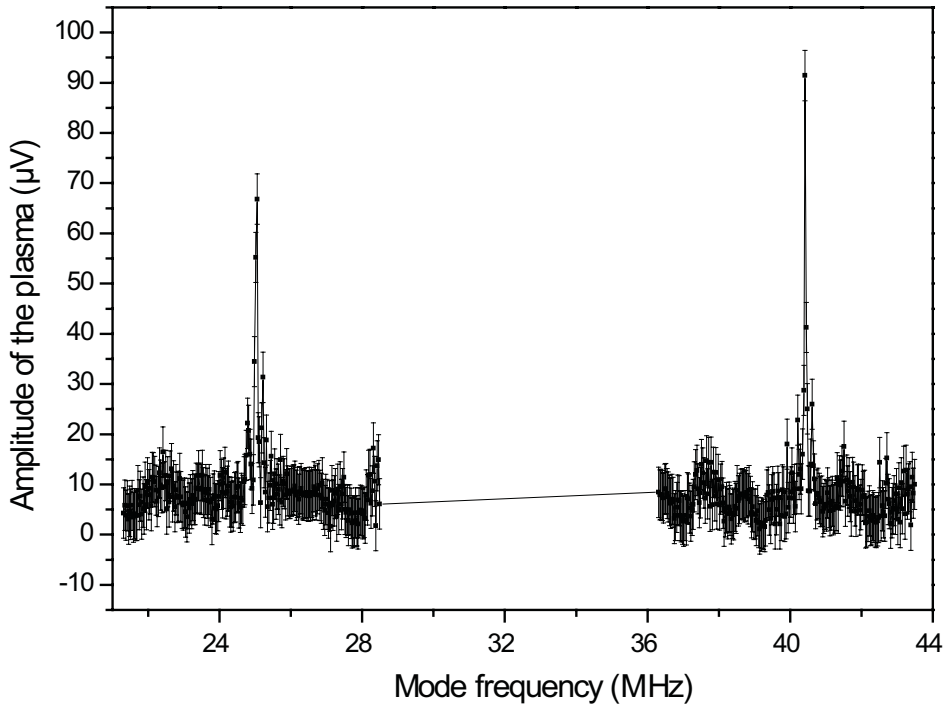

Fig. 4.3: First two plasma modes, recorded with the plasma modes diagnostics system.

which yielded a value of 15.59 for α. Overall the Labview program output was found to be very trustworthy.

4.3 Free plasma evolution

Next the long-term behavior of the plasma in the trap was examined. For this purpose the plasma was captured and then simply left to evolve on its own, while being measured at regular intervals. An interesting measurement of free plasma evolution is the observation of density as a function of time, which is shown in Figure 4.6. As can clearly be seen in the figure, the density of the plasma decreases approximately linearly with time. The four data sets correspond to four different magnetic fields: 2 T, 3 T, 4 T and 4.8 T. The behavior of the density with time seems to be independent of the applied magnetic field, since the density decreases similarly at all four magnetic field intensities. In the case of the data set for 2 T, the initial density was a little larger due to the fact that more particles were trapped from the beginning. The uncertainty of the graphs corresponds to 10% of the

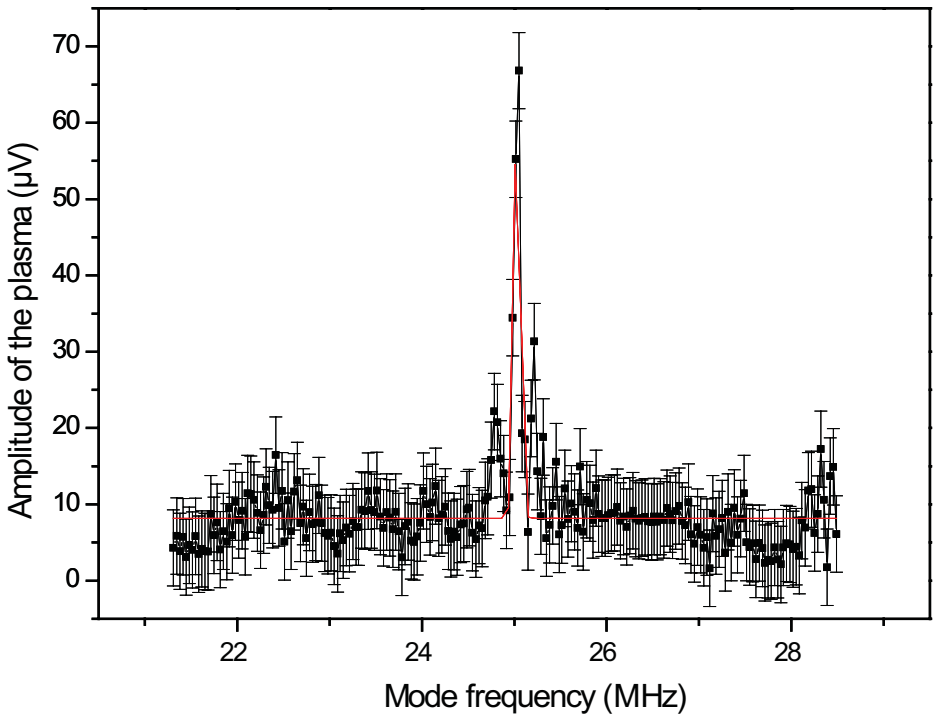

Fig. 4.4: Gaussian fit of the first mode.

measured value because the density is calculated from the numerically calculated aspect ratio α, which already contains an uncertainty of the measured frequencies ω_1 and ω_2. Our mode analyzer was also used in the ATHENA experiment, where an uncertainty of the same order of magnitude has been supposed [29].

Further, the plasma size is of interest. The radii were measured only respectively to one another because to conduct an absolute measurement a calibration of the exact number of particles would have to be done. The behavior of the radii of the trapped plasma with time at different magnetic fields is represented in Figures 4.7 and 4.8.

It can be seen that the elliptical semi-minor axis R_p grows with time while the elliptical semi-major axis Z_p shrinks, which means that the plasma becomes smaller in the axial direction and wider in the radial direction. This is consistent with the measurements of the ATHENA experiment [27]. Again the behavior seems to be independent of the applied magnetic field since the radii increase and decrease similarly at all magnetic field strengths. The uncertainty corresponds again to 10% of the measured value, because the radii are calculated from the density which itself has an uncertainty of 10%.

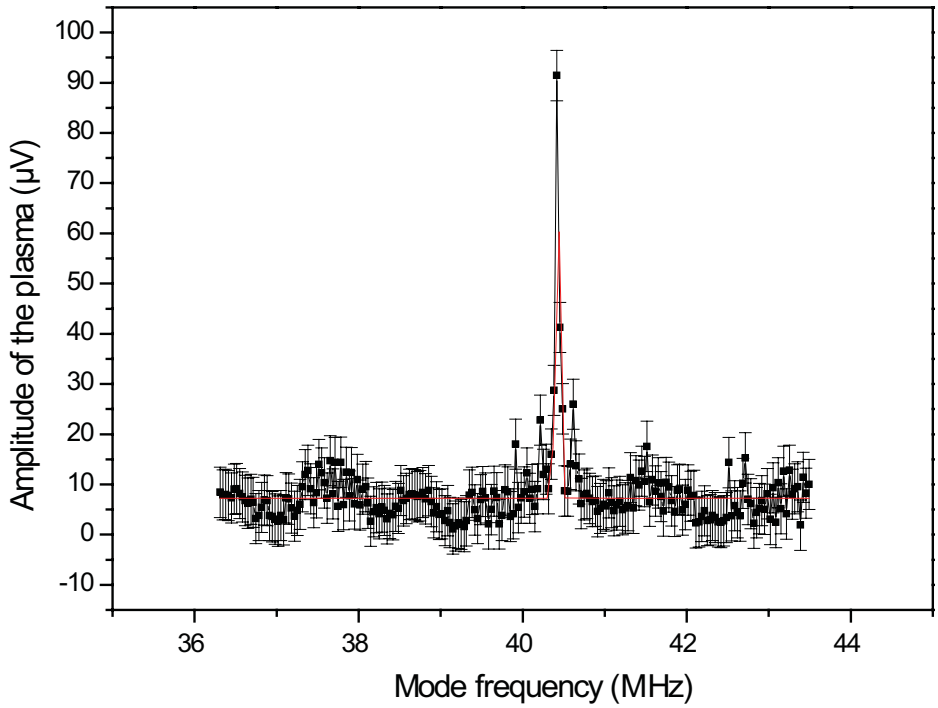

Fig. 4.5: Gaussian fit of the second mode.

The behavior of the two radii implies that the aspect ratio α, that is the ratio of the two radii, has to decrease perceptibly at the same time. This can be nicely seen in Figure 4.9. Here also the uncertainty was assumed to be 10% of the measured value. As before the strength of the magnetic field has no marked effect on the evolution of the aspect ratio. Our measurements show that it is possible to trap a plasma for more than 200 s and to examine it non-destructively.

Further measurements showed that it was even possible to store and non-destructively examine the plasma for up to 400 s. Only then will the plasma not be detected any more. This could either be due to the fact that more and more particles escape by radial losses, or to the fact that the plasma continues to expand more and more and at some point the semi-minor axis R_p equals the Debye length. In this case it is not a plasma any more, but only a collection of particles which do not behave collectively.

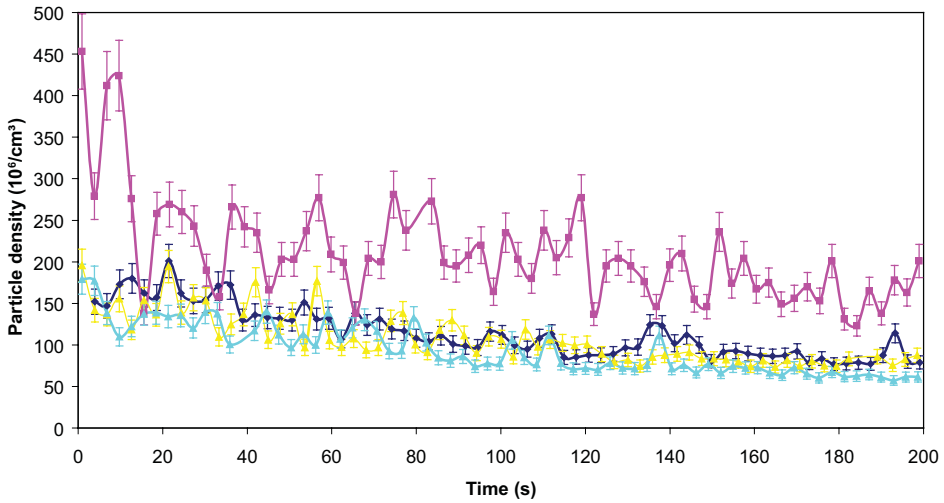

Fig. 4.6: Particle density as a function of time at four different magnetic field magnitudes: 2 T (magenta), 3 T (yellow), 4 T (light blue), 4.8 T (dark blue).

4.4 Dependence of the frequency on the trap potential

Next, the dependence of the first mode frequency on the depth of the applied trap potential was tested. From Equation (2.17), a square root dependence on the trap potential can be expected, which is confirmed by the measurement shown in Figure 4.10. The fitted graph is compatible with a square root function. The uncertainties of the values are based on our measurement uncertainties in addition to the frequency uncertainties of 1 kHz, measured in Genoa, and are therefore about 0.5 MHz. When comparing this result with that of a single particle, we see that the frequency of a single particle would be considerably higher than is the one of the plasma, which is due to the coherent plasma motion. It is therefore remarkable that the plasma behaves just as a single particle concerning the dependence on the trap potential.

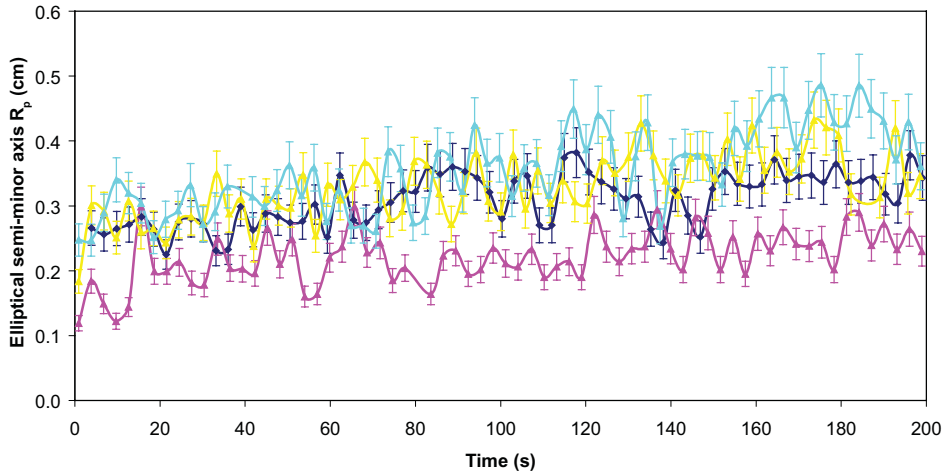

Fig. 4.7: Elliptical semi-minor axis R_p of the freely evolving plasma at different magnetic fields.

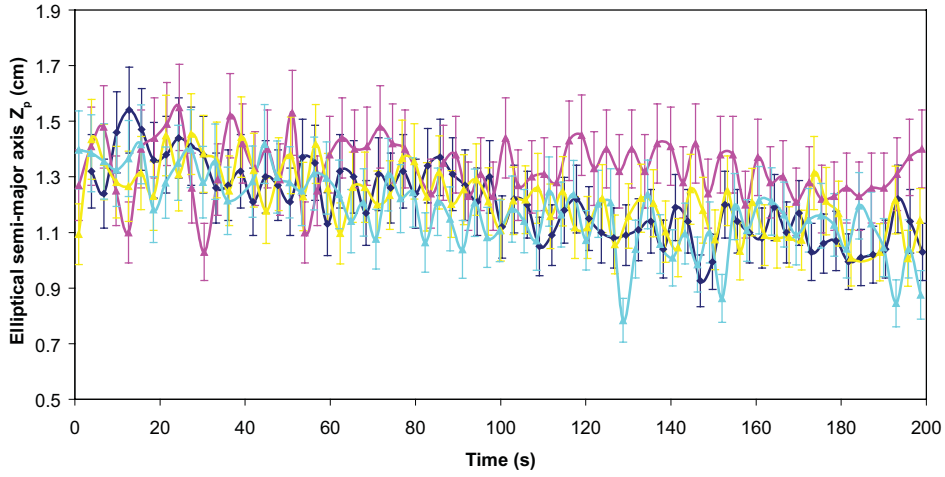

Fig. 4.8: Elliptical semi-major axis Z_p of the freely evolving plasma at different magnetic fields.

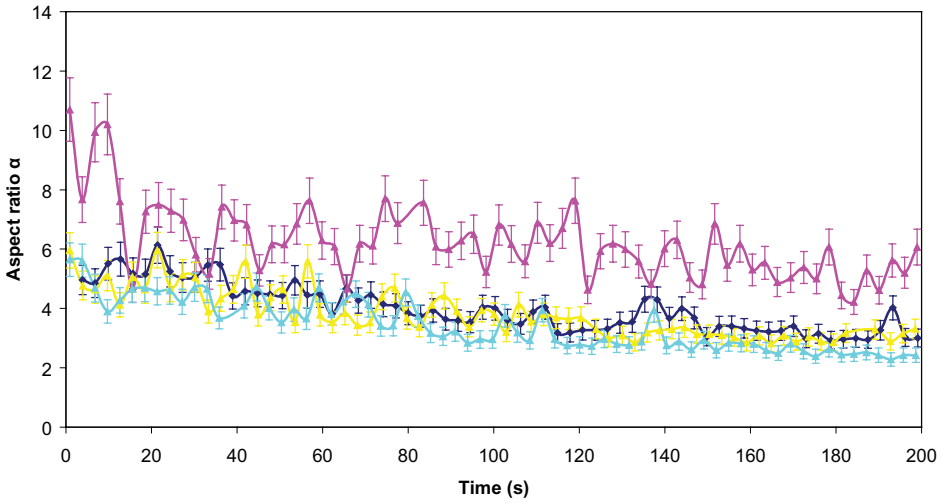

Fig. 4.9: Aspect ratio α of the freely evolving plasma as a function of time at four different magnetic field magnitudes: 2 T (magenta), 3 T (yellow), 4 T (light blue), 4.8 T (dark blue).

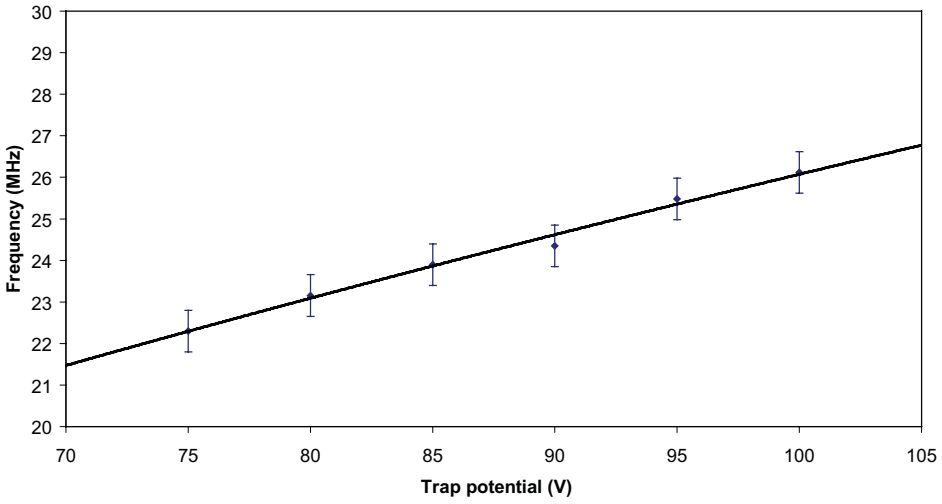

Fig. 4.10: First plasma mode frequency as a function of the trap potential. The black line is a square root fit to the data.

5. PLASMA MANIPULATION

5.1 Heating of the plasma

Next, we further examined plasma properties by disturbing the plasma. For this purpose, we used a frequency generator that excited the first plasma mode in a frequency sweep from 24 to 26 MHz and thereby modulated the additional voltage on the ring electrode by 0.2 to 0.9 V. This induced a heating of the plasma, as it was excited and thereby gathered energy. The frequency range from 24 to 26 MHz was repeatedly traversed in steps of 1 kHz.

The heating process of the plasma can be studied by examining the subsequent cooling process as a function of the magnetic field of the Penning trap. Therefore we had to excite the plasma at different magnetic fields, producing the graph shown in Figure 5.1. In this figure there is a clear rise of the frequency as soon as the frequency generator was switched on (time $t \approx 2.8$ s) and the plasma was heated. The heating was done at the frequency of the first plasma mode, and the second mode was measured during the heating process. Because the excitation was done in the frequency range of the first mode, measuring the first mode during the process was not possible. In the second mode, an exponential decay can be seen, from which the cooling rate can be obtained. To do this the decay is fitted with an exponential function. The cooling time τ can be calculated from the synchrotron radiation [30]:

$$\frac{dE_\perp}{dt} = \frac{2e^2}{3c^3} a_\perp^2 = \frac{4e^2\Omega^2}{3mc^3} E_\perp, \tag{5.1}$$

where $a_\perp = \Omega v_\perp$ is the perpendicular acceleration and $E_\perp = mv_\perp^2/2$ the perpendicular energy. Averaging Equation (5.1) over a Maxwellian distribution yields

$$\frac{dT_\perp}{dt} = -\frac{3T_\perp}{2\tau}, \tag{5.2}$$

with

$$\tau = \frac{9mc3}{8e^2\Omega^2} \approx \frac{4 \times 10^8}{B^2}. \tag{5.3}$$

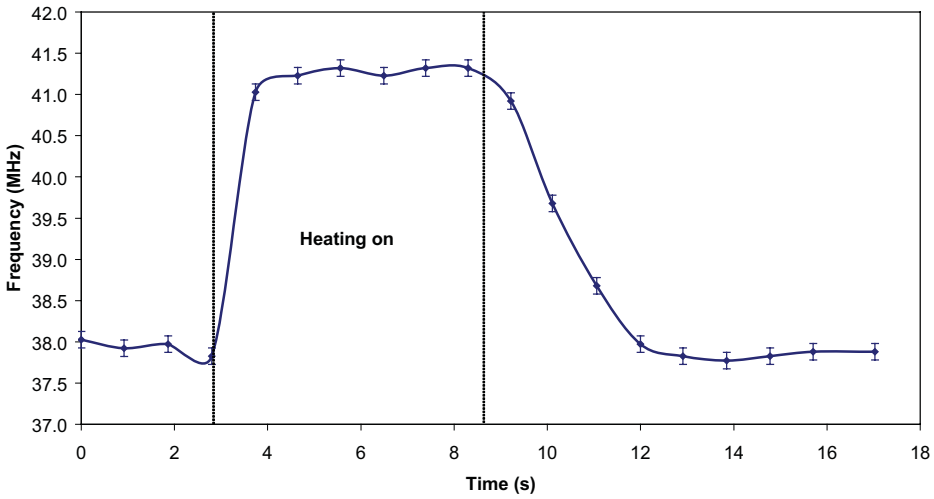

Fig. 5.1: Plasma frequency before, during and after the heating. At the end of the heating an exponential decay back to the starting plasma frequency is observed.

The cooling rates measured at different magnetic fields with an excitation amplitude of 0.5 V are shown in Figure 5.2. The plotted uncertainty is that of the fitting process and therefore smaller than the actual uncertainty, since the fitted values in themselves already contain uncertainties. Figure 5.2 shows that our data qualitatively agree with the theoretical result. The main difference is that our measurement shows a higher cooling rate than theory predicts in each case. A possible reason could be the presence of other heating mechanisms, such as excitation by stray fields. This result is supported by other measurements [30], where heating from unknown mechanisms also occured.

Another examined plasma property was the temperature increase as a function of the applied excitation amplitude. According to Tinkle et al. [31] and Amoretti et al. [32] the temperature change ΔT of the plasma is given by

$$k\Delta T = \frac{mZ_p^2}{5}\left[(\omega_2^h)^2 - (\omega_2)^2\right]\left[3 - \frac{\omega_p^2\alpha^2}{2\omega_2^2}\frac{d^2 f(\alpha)}{d\alpha^2}\right]^{-1}, \tag{5.4}$$

with $f(\alpha) = 2Q_1^0(\alpha/\sqrt{\alpha^2-1})/(\alpha^2-1)$ and ω_2^h the second mode frequency during the heating process. This relation shows that the change in temperature not only depends on the density (via the plasma frequency ω_p) and the aspect ratio α, but also on the plasma length Z_p (the semi-major axis). For the purpose of this measurement, we used the measured values for α between 18.91 and 20.68 and Z_p between 0.4079 cm and 0.4977 cm,

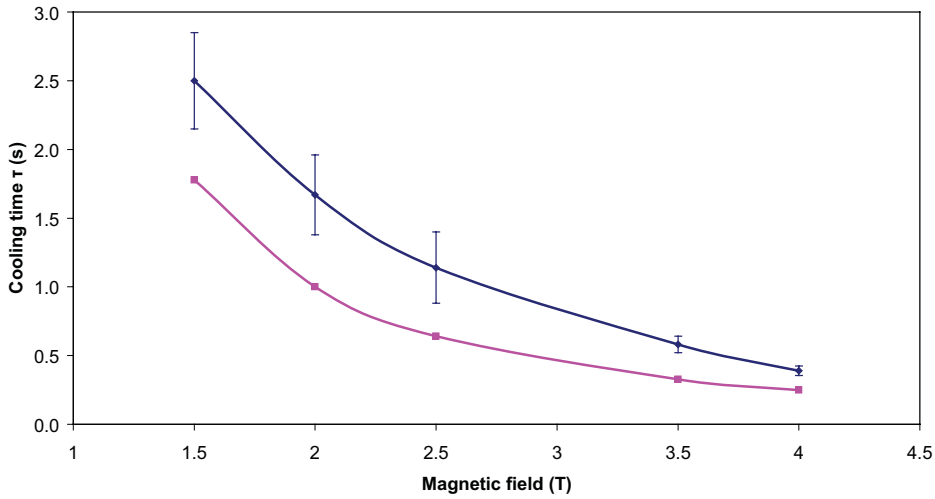

Fig. 5.2: Cooling time for different magnetic fields for the same heating process of the plasma. The magenta line is the theoretical expectation and the dark blue line our experimental result.

Z_p being only a relative value as already mentioned in Section 4.1. For the heating process at different voltages that are shown in Figure 5.3, we obtain the temperature increases shown in Figure 5.4. In Figure 5.3 the increase of the frequency at higher heating voltages is clearly visible. The heating voltages are increased in steps of 0.1 V from 0.2 V (almost not visible) up to 0.9 V. Our results show that the temperature change increases approximately linearly with the heating voltage. The uncertainty of our values was assumed to be 10%, as was the case in the ATHENA experiment.

This linear dependency is consistent with the measurements of ATHENA [32], although, as mentioned there too, a quadratic dependency had been expected due to the fact that $k\Delta T$ is in units of energy and hence expected to be proportional to V_d^2. In the ATHENA experiment a temperature increase greater than ours by a factor of 10 was obtained with a heating voltage lower than we used by a factor of 100. This difference can be due to the fact that positrons constituted the plasma of ATHENA, resulting in fewer particles and lower density. Further a smaller-diameter Penning trap was used in the ATHENA experiment and the semi-major axis Z_p of the plasma was greater by more than a factor of 3. Also different cable lengths lead to different attenuations of the radio frequency signals. All in all, however, we can confirm the approximately linear dependency of the temperature shift on the heating voltage, as it was also measured in the ATHENA experiment.

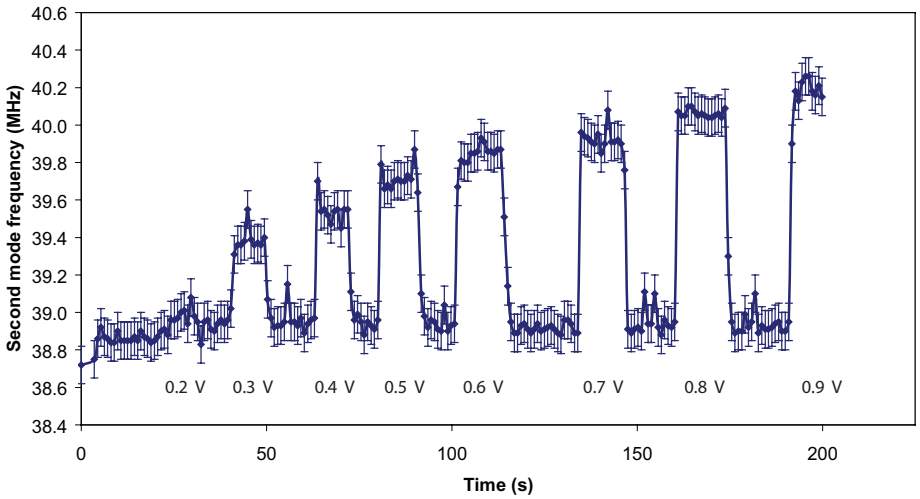

Fig. 5.3: Changes in the second mode frequency for different heating voltages. The higher the heating voltage the higher the increase of the frequency that is seen. The heating voltage was increased from 0.2 V to 0.9 V in steps of 0.1 V.

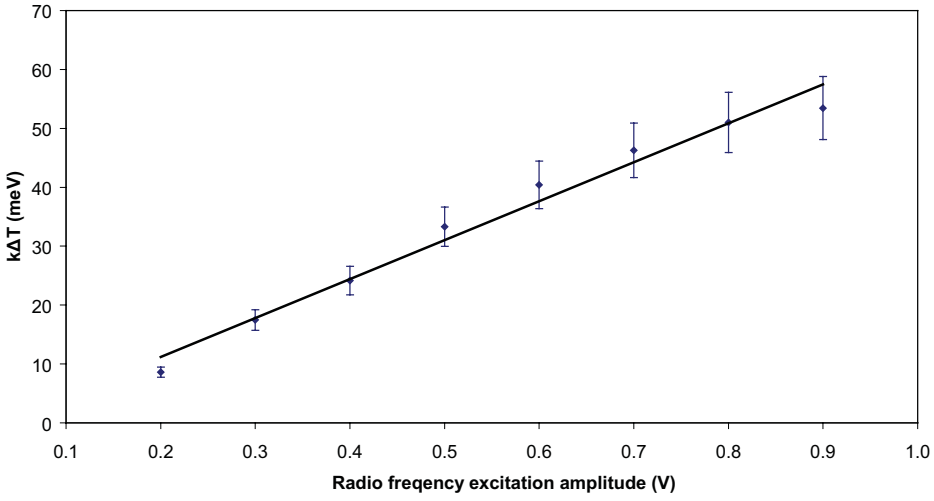

Fig. 5.4: Temperature shift for different heating voltages. The solid line is meant to guide the eye.

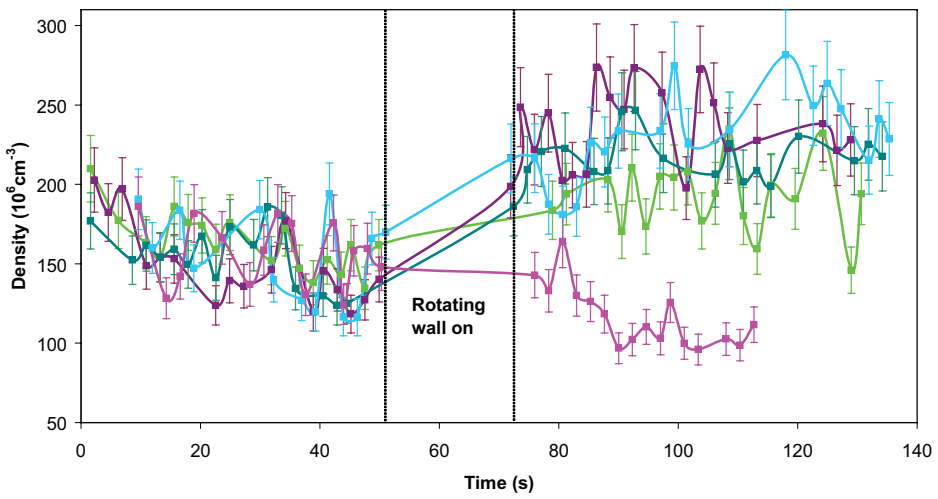

Fig. 5.5: Plasma density for different amplitudes of the rotating wall. The amplitudes were increased from 2 V to 10 V in steps of 2 V: 2 V (magenta), 4 V (green), 6 V (purple), 8 V (teal), 10 V (light blue). The transition region between weak and strong drive can be seen.

5.2 Rotating wall

The last measurements performed in the course of this work concerned a rotating wall excitation. As was shown in Section 2.4, a rotating wall excitation compresses or expands the plasma in the radial direction [33]. Compression may be used to increase the time period that the plasma can be stored for. We then studied the behavior of the plasma density as a function of the excitation amplitude that is applied to the electrode segments. Our measurements were done at a direct current voltage of 100 V, a magnetic field of 4.8 T and a rotating wall frequency of 6 MHz for a duration of 20 s. No measurement data could be recorded during the operation of the rotating wall. The result is shown in Figure 5.5. Here the different applied excitation amplitudes from 2 V to 10 V are shown by data points in different colors. The marked uncertainties are again 10%. The 2 V amplitude does not induce a change of density, while at 4 V a distinct compression of the plasma begins to appear. The behavior at the amplitudes 6 V, 8 V and 10 V is nearly the same and we record roughly the same plasma density after compression. Only at an applied voltage of 4 V do we observe a final density that is a bit lower than the others, which leads to the assumption that this voltage lies exactly in the transition region between the weak and the strong drive, as was the case in the work of Danielson et al. for an amplitude of 0.7 V [33].

The density achieved by compression as a function of the applied excitation amplitude

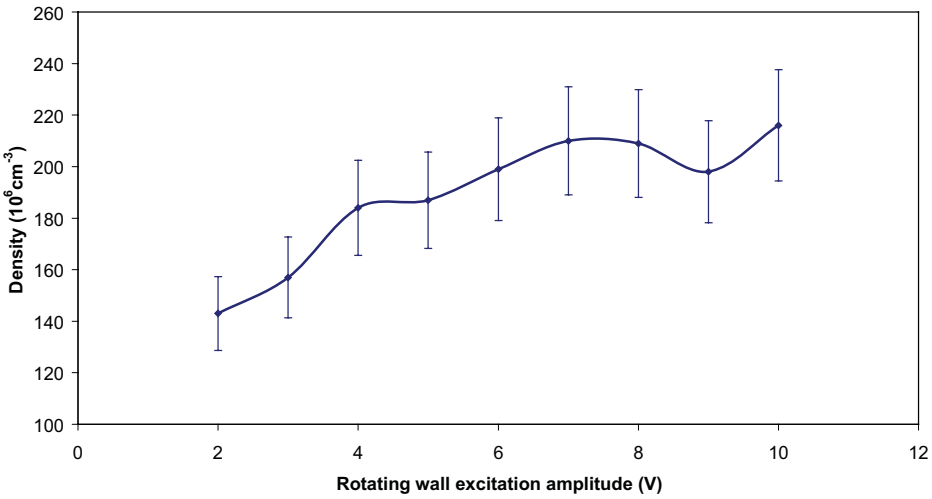

Fig. 5.6: Final steady-state density as a function of the rotating wall amplitude.

is shown in Figure 5.6. This figure also shows a very good agreement with another work by Danielson et al. [34]. However, they also found that for very small rotating wall amplitudes of about 0.3 V and less, the density slowly tends to zero. We have not examined this amplitude regime. The results of the ATHENA experiment also show a similar trend for the compression as a function of the excitation amplitude [29]. All in all, the comparisons show a good agreement between the different experiments.

Another quantity of interest is the density change of the plasma as a function of the different frequencies of the rotating wall. For this we conducted two measurements at a magnetic field of 2 T for a rotating wall amplitude of 6 V during 25 s. The tested frequencies were 6 and 7 MHz. During the operation of the rotating wall, no density data were recorded. The resulting graph is shown in Figure 5.7. A rise in the density after the rotating wall is clearly discernable, which suggests that the excitation is working as expected. The dependence of the final plasma density on the applied frequency should have been linear, as for Danielson et al. [34], but since we only observed the density for the two frequencies indicated above, a linear fit to these data is not meaningful.

Finally we considered whether particles can be stored longer with the repeated operation of a rotating wall and the following compression. All important plasma properties were measured at a magnetic field of 2 T and a trap depth of 85 V with and without the rotating wall at a frequency of 6 MHz and an amplitude of 6 V in intervals of 30 s each including a 10 s rotating wall excitation. The results are shown in Figures 5.8 and 5.9. In

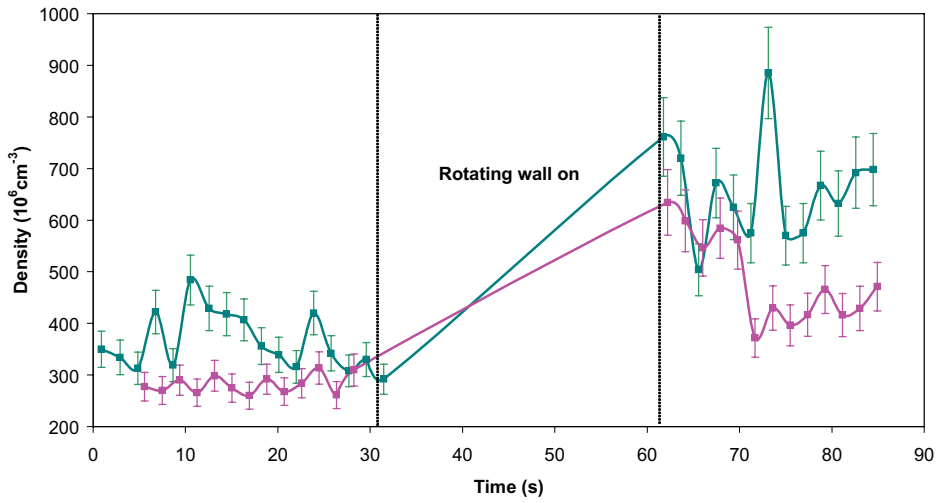

Fig. 5.7: Plasma density as a function of time for rotating wall frequencies of 6 MHz (magenta) and 7 MHz (green).

Figure 5.8 one can observe that without the rotating wall the density decreases during the first 200 s. Afterwards plasma instabilities occur and some electrons are lost, while the rest of the electrons apparently move closer together. This causes an increase in density during the following 80 s, until there is only noise left. This is different with the rotating wall, where the plasma is first compressed, inducing the density to rise during the first 150 s and then to stay constant. In this way, the plasma can evidently be stored longer. The measured aspect ratio α behaves exactly the same as the density's trend, and the remarks concerning the density apply accordingly.

In Figure 5.9 the semi-minor axis R_p is shown to rise during the first 200 s without the rotating wall, while it falls during the following 80 s and can finally not be measured any more. This supports the above supposition about the behavior of the plasma. With the rotating wall R_p contracts a bit in the beginning and then stays virtually constant, which agrees with the trend of the plasma density and the aspect ratio. We can thus infer that the plasma can be stored significantly longer with the rotating wall. Our measurements show that the plasma can be stored only for about 200 s without the rotating wall, whereas with the rotating wall it is not lost during the entire observation time of 1000 s. Since the plasma parameters showed almost no fluctuations during the last 800 of these 1000 s, we can assume that a storage of the plasma for longer than that time period should certainly be possible.

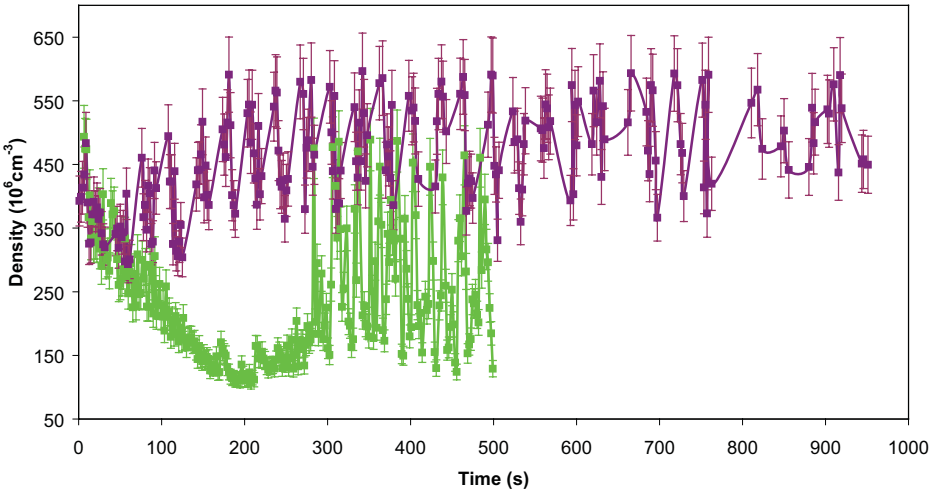

Fig. 5.8: Plasma density as a function of time with (magenta) and without (green) the rotating wall. The magenta line shows a small increase of the density and then the density is constant with the rotating wall. The line without the rotating wall first shows a decrease of the density and then a short increase up to the point where the plasma could not be detected any more ($t \approx 300$ s; the fluctuations between $t \approx 300$ s and 500 s are due to noise).

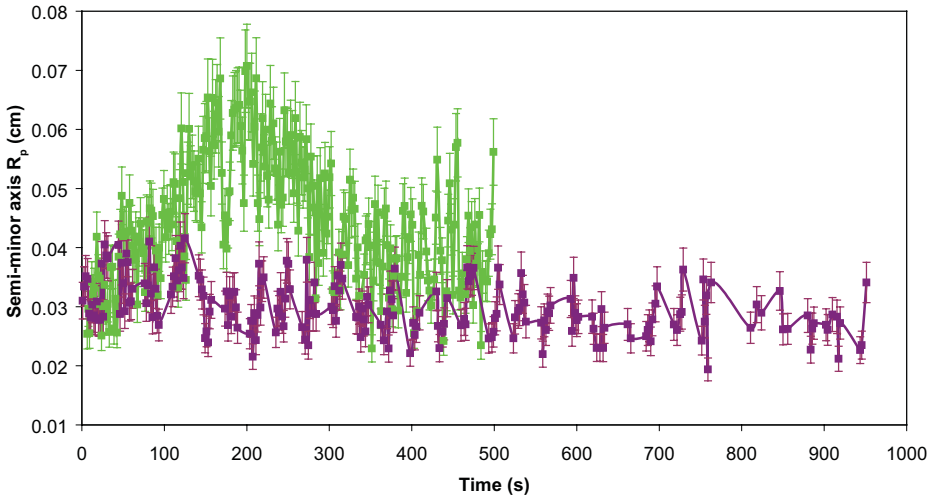

Fig. 5.9: Semi-minor axis R_p as a function of time with (magenta) and without (green) the rotating wall excitation.

6. CONCLUSION

In this diploma thesis, the creation, diagnostics and manipulation of an electron plasma, from the construction of an electron source to the excitation of electrons confined in a Penning trap, has been described. First, an electron gun was designed around a pre-existing BaO electron source, such that the electrons created in the source could be formed into a beam. Several different designs of the electron gun were considered, virtually constructed with the program SolidWorks and the electron trajectories simulated with Simion. The best simulated result, with a theoretical efficiency of 100%, was then constructed in reality and tested.

The attention was then directed to the task of creating a plasma in the Penning trap. For this purpose, the electron beam was captured and confined in the Penning trap, whose construction was completed in the course of this thesis. With a plasma mode analyzer, based on a design from the University of Genoa, the first plasma measurements were conducted. Different loading procedures were first tested to capture as many electrons as possible. Afterwards the output of the mode analyzer was tested and confirmed with a manual analysis. Subsequently the evolution of the plasma with time was examined and it was tested how the different plasma parameters, like the density, the aspect ratio and the radii, behaved. Then the behavior of the plasma that had been disturbed by heating with a radio frequency was examined. After the heating process the cooling time was determined at different magnetic field strengths. Finally the plasma was excited by an applied rotating wall electric field. Thus it was compressed and the plasma stored for a longer time. This compression was ascertained by means of the plasma parameters and a storage time of up to 1000 s was found.

In summary, an electron plasma was successfully created and confined in a Penning trap. The plasma diagnostics apparatus was installed and used to measure the most important plasma parameters. Excitation of the plasma by radio frequency heating and rotating wall excitation was shown to yield results compatible with expectations from theoretical calculations and prior experiments. Hence, the goals of this thesis work have been fulfilled, paving the way for the further use of the electron plasma as part of the UNIC project.

BIBLIOGRAPHY

[1] W. Pauli, in: Niels Bohr and the development of physics, New York: Pergamon (1955), p. 30.

[2] P. B. Schwinberg et al., Phys. Lett. A 81 (1981) 119.

[3] G. Gabrielse et al., Phys. Rev. Lett. 82 (1999) 3198.

[4] R. S. Van Dyck, Jr. et al., Phys. Rev. Lett. 59 (1987) 26.

[5] G. W. Bennett et al., Phys. Rev. Lett. 92 (2004) 161802.

[6] G. Gabrielse et al., Phys. Rev. Lett. 98 (2007) 113002.

[7] G. Andresen et al., Phys. Rev. Lett. 98 (2007) 023402.

[8] M. Niering et al., Phys. Rev. Lett. 84 (2000) 5496.

[9] M. Amoretti et al. (ATHENA Collaboration), Nature 419 (2002) 456.

[10] G. Gabrielse et al. (ATRAP Collaboration), Phys. Rev. Lett. 89 (2002) 213401.

[11] G. Galilei, Discorsi e dimostrazioni matematiche, intorno a due nuove scienze, Leiden: Elsevier (1638).

[12] E. G. Adelberger, B. R. Heckel and A. E. Nelson, Ann. Rev. Nucl. Part. Sci. 53 (2003) 77.

[13] A. Kellerbauer et al., Nucl. Instrum. Methods B 266 (2008) 351.

[14] C. M. Surko, M. Leventhal and A. Passner, Phys. Rev. Lett. 62 (1989) 901.

[15] D. W. Gidley, H.-G. Peng and R. S. Vallery, Annu. Rev. Mater. Res. 36 (2006) 49.

[16] M. Charlton, Phys. Lett. A 143 (1990) 143.

[17] E. Vliegen et al., Phys. Rev. A 76 (2007) 023405.

[18] M. K. Oberthaler et al., Phys. Rev. A 54 (1996) 3165.

[19] A. Kellerbauer and J. Walz, New J. Phys. 8 (2006) 45.

[20] R. C. Bilodeau and H. K. Haugen, Phys. Rev. Lett. 85 (2000) 534.

[21] C. Carraro, Progettazione e tests del sistema di cattura e rivelazione per l'esperimento ATHENA, Diploma thesis, University of Genoa (2000).

[22] H. Raimbault-Hartmann et al., Nucl. Instrum. Methods B 126 (1997) 378.

[23] L. Brown, G. Gabrielse, Rev. Mod. Phys. 58 (1986) 233.

[24] M. Tinkle, R. Greaves, C. Surko, Phys. Plasmas 2 (1995) 2880.

[25] D. Dubin, Phys. Rev. Lett. 66 (1990) 2076.

[26] D. Dubin, Phys. Fluids B 5 (1993) 295.

[27] C. Carraro, Charged particles manipulation and diagnostic for sub-eV antihydrogen production in ATHENA experiment, PhD Thesis, University of Genoa (2004).

[28] K. Reisinger, Emittance Measurements on the Sideband Cooling Technique and Introduction of the Rotating Wall Cooling Technique at REXTRAP, Diploma Thesis, Technical University of Munich (2002).

[29] R. Funakoshi et al., Phys. Rev. A 76 (2007) 012713.

[30] B. Beck, J. Fajans, J. Malmberg, Phys. Plasmas 3 (1996) 1250.

[31] M. Tinkle, R. Greaves, C. Surko et al., Phys. Rev. Lett. 72 (1994) 352.

[32] M. Amoretti et al., Phys. Plasmas 10 (2003) 3056.

[33] J. Danielson, C. Surko, Phys. Plasmas 3 (2006) 1250.

[34] J. Danielson, C. Surko, T. O'Neil, Phys. Rev. Lett. 99 (2007) 135005.

[35] M. Amoretti et al., Phys. Rev. Lett. 91 (2003) 055001.

[36] J. Meier, Matching of the beam from a negative-ion source for capture in a Penning trap, Diploma thesis, University of Heidelberg (2007).

[37] H. Zhong, Nucl. Instrum. Methods A 463 (2000) 250.

[38] M. Amoretti, Nucl. Instrum. Methods A 518 (2004) 679.

ACKNOWLEDGMENTS

With the last sentences of this thesis I want to mention those people who made my work and writing this thesis extraordinarily simpler for me during this last year.

First of all, it is my dear pleasure to thank Alban Kellerbauer for supervising my diploma thesis and thereby giving me the possibility to work at the Max Planck Institut for nuclear physics on a very interesting topic. I want to further thank him for the advice and ameliorations during the creation process of this diploma thesis.

In addition I wish to thank Selim Jochim who agreed to be the second corrector of this thesis and I wish to thank Carlo Canali with whom I have conducted a lot of measurements and who provided me with plenty of background information.

For the good collaboration I would like to thank my work group of the UNIC project and the employees of the MPIK without whom the realisation of this project would not have been possible. The members of my work group are Arne Fischer, Ulrich Warring, Christoph Morhard and Carlo Canali. Special thanks I would like to give to Mr. Mallinger and Mr. Beckmann who have been a great and fast help with all the constructions. Furthermore I want to thank the staff of the electronic and the material distribution section who kindly turned a blind eye every once in a while outside normal working hours and gave out materials nevertheless.

Then I want to give special thanks to my parents, Rudolf and Regina Heyne, who rendered my studies possible in the first place.

Thanks is also due to my fellow students who have contributed a lot to the fact that my years of study will always be remembered favorably by me and who have always helped me with words and deeds in all life situations. Among these people are Sandra Tomschin, Bastian Jungnitsch, Eike Nicklas and Mischa Gerstenlauer. My co-workers of KST-Motorenversuch and by now several other companies I would like to thank because on the one hand they made my living standard possible, as I could work for them, and on the other hand they helped me a lot and showed me a different side of (work) life. These people are Marc Bary, Knut Beller, Volker Liebler and Jan Fürstenberger. Further I would like to thank every other person that I have not mentioned by name in this paragraph.

Finally I wish to thank my girlfriend Anna Lena Baumann who gave me a lot of strength during this thesis and who has always been by my side emotionally and morally although the work on this thesis has separated me from her more than once. I love you.

ERKLÄRUNG:

Ich versichere, dass ich diese Arbeit selbstständig verfasst und keine anderen als die angegebenen Quellen und Hilfsmittel benutzt habe.

Heidelberg, den 31.10.2008